# Full-Duplex 60 GHz Band Dense Wavelength Division Multiplexing Star Tree Architecture For Radio-Over-Fiber Systems

Baozhu Liu

A Thesis

In

The Department of Electrical and Computer Engineering

Presented in Partial Fulfillment of the Requirements

For the Degree of Master of Applied Science at

Concordia University

Montreal, Quebec, Canada

December 2004

*Your file Votre référence*
*ISBN: 0-494-04383-0*
*Our file Notre référence*
*ISBN: 0-494-04383-0*

## ABSTRACT

Full-Duplex 60 GHz Band Dense Wavelength Division Multiplexing Star Tree Architecture For Radio-Over-Fiber System

Baozhu Liu

In this work, full-duplex 60GHz DWDM star tree architecture for radio-over-fiber systems is investigated. New approach by using DWDM with the channel spacing of 25 GHz for the first time is proposed to improve the spectral efficiency. The demonstration system consists of 1 central station and 3 base stations as an example. In addition, the remote light source technique is utilized to simplify the architecture of base station (BS) and the external modulation technique is adopted to overcome the fiber chromatic dispersion. Especially, the MZ modulator, configured to generate optical single sideband (OSSB) signal, is adopted in the central station and modulates the optical carrier with the lower sideband (LSB) and upper sideband (USB) subcarriers simultaneously with different data and the EA modulator is adopted in the base station for implementing the maintenance-free BS in the future.

The error-free transmission via the 25 km uplink and downlink fiber with the data rate of 155.52 Mbps is performed. The impact of the laser linewidth and the bandwidth of the electrical bandpass filter are investigated. It concludes that the system performance is limited by the laser phase noise for considered DPSK signal and the bandwidth of electrical bandpass filter is much larger than the 3-dB bandwidth. The trade-off has to be made when optimizing the laser linewidth and the bandwidth of the bandpass filter.

# ACKNOWLEDGEMENTS

First all, I would like to express my appreciation and thankfulness to my research advisor Professor Dr John X. Zhang for his supervision and valuable advise over the past two years. His bright idea and encouraging suggestion make me overcome the challenge I encountered during my research and achieve the result described in this work at last.

In addition, I would like to thank the Canadian Institute for Photonic Innovation (CIPI) and Faculty of Electrical and Computer Science Engineering at Concordia University to support this project.

Moreover, I would like to thank for the valuable discussion with my classmate: Lei Wang.

Finally, I would like to thank my wife, Hui Zhang, and two children, Haoyu Liu and Haoan Zhang, for their love and support during my research.

# TABLE OF CONTENTS

# LIST OF FIGURES

# LIST OF TABLES

# LIST OF ABBREVIATIONS

| | |
|---|---|
| ASK | Amplitude shift keying |
| BER | Bit error rate |
| BS | Base station |
| CS | Central station |
| DPSK | Differential phase shift keying |
| DSB | Double sideband |
| DWDM | Dense wavelength division multiplexing |
| FSK | Frequency shift keying |
| LSB | Lower sideband |
| OSSB | Optical single sideband |
| PD | Photo detector |
| PRBS | Pseudorandom bit sequences |
| RN | Remote node |
| RF | Radio frequency |
| ROF | Radio-over-fiber |
| SMF | Single mode fiber |
| SSB | Single sideband |
| USB | Upper sideband |

# LIST OF SYMBOLS

| | |
|---|---|
| $C_n$ | The nth channel of optical carrier |
| $c$ | Light speed in the vacuum |
| $\lambda_{cn}$ | Wavelength of the nth optical channel $C_n$ |
| $dn$ | Subscript for the downlink parameter at the nth optical channel $C_n$ |
| $un$ | Subscript for the uplink parameter at the nth optical channel $C_n$ |
| $cn$ | Subscript for the parameter of the nth optical channel $C_n$ |
| $f_{cn} = c/\lambda_{cn}$ | Frequency of the nth optical channel $C_n$ |
| $f_d$ | Downlink radio frequency |
| $f_{dn}$ | Downlink radio frequency for the nth optical channel $C_n$ |
| $f_u$ | Uplink radio frequency |
| $f_{un}$ | Uplink radio frequency for the nth optical channel $C_n$ |
| $U_n$ | USB subcarrier of the nth optical channel $C_n$ |
| $L_n$ | LSB subcarrier of the nth optical channel $C_n$ |
| $f_{cn} + f_d$ | Frequency of the USB subcarrier of the nth optical channel $C_n$ |
| $f_{cn} - f_d$ | Frequency of the LSB subcarrier of the nth optical channel |

| | |
|---|---|
| | $C_n$ |
| $f_{ch}$ | Channel spacing of DWDM |
| $e_{cn}(t)$ | Electrical field signal of the nth optical channel $C_n$ |
| $P_{cn}$ | Optical power of the nth optical channel $C_n$ |
| $\phi_{cn}(t)$ | Phase noise of the optical carrier $C_n$ |
| $m_{dn}(t)$ | Downlink electrical USB signal of the optical carrier $C_n$ |
| $V_{dn}$ | Amplitude of downlink electrical USB and LSB signal |
| $\theta_{dn}(t)$ | Payload data of downlink USB signal |
| $m_{dn}^{'}(t)$ | Downlink electrical LSB signal |
| $\theta_{dn}^{'}(t)$ | Payload data of downlink LSB signal |
| $\beta\pi = \pi V_{ac} / V_{\pi}$ | Normalized amplitude of the RF drive signal |
| $V_{ac}$ | Amplitude of RF signal |
| $V_{\pi}$ | Switching voltage of the MZ modulator |
| $J_0$ | The zeroth term of Bessel function |
| $J_1$ | The first-order term of Bessel function |
| $a_{opt}$ | Bifurcation ratio of the optical power divider |
| $X_d$ | Downlink fiber length |
| $X_u$ | Uplink fiber length |
| $\beta_{d,n}(f)$ | Propagation constant of the downlink fiber |
| $\beta_{u,n}(f)$ | Propagation constant of the uplink fiber |

| | |
|---|---|
| $D_{d,n}$ | Fiber dispersion parameter of the downlink fiber |
| $D_{u,n}$ | Fiber dispersion parameter of the uplink fiber |
| $\psi_{p,n}(t, X_d)$ | Phase of the *pth* order component of the nth downlink optical carrier $C_n$ |
| $i_{cn,L(n+2)}(t, X_d)$ | Downlink photocurrent of beating signal between the optical carrier $C_n$ and the subcarrier $L_{n+2}$ |
| $\psi_{cn,L(n+2)}(t, X_d)$ | Phase difference of the optical carrier $C_n$ and the subcarrier $L_{n+2}$ |
| $m_{un}(t)$ | Uplink electrical signal |
| $\theta_{un}(t)$ | Payload data of uplink signal |
| $i^{uplink}_{c(n+2),Ln}(t, X_d, X_u)$ | Uplink photocurrent of beating signal between the optical carrier $C_{n+2}$ and the subcarrier $L_n$ |
| $v_{0,r,n}(t, X_d, X_u)$ | Phase of the *rth* component of the *nth* uplink optical carrier $C_n$ |
| $\psi_{c(n+2),Ln}(t, X_d, X_u)$ | Phase difference of the uplink optical carrier $C_{n+2}$ and the subcarrier $L_n$ |

# Chapter 1 Introduction

In order to provide the broadband service, the available bandwidth of radio frequency always is an issue to be resolved at first. Many projects and programs across the world are undergoing to explore where the radio frequency can be allocated with large trunk of bandwidth to have the broadband services implemented [1]. In Europe, the 19, 40 and 60 GHz bands have been addressed under different projects. In Japan, the 40 and 60 GHz attract the interest in the research community to implement the dense local wireless LANs. In US, FCC reserves the 59-64 GHz for future unlicensed application of wireless access system. In general, there is about 8-GHz bandwidth available for dense wireless access communications. Therefore, the 60 GHz band brings up of utmost interest for all kinds of short-range wireless communications.

The 60 GHz bands operating in the $4^{th}$ generation wireless system feature high density because of the pico-cell architecture. In order to deliver the radio signal, the cost-effective technology and system have to be developed to address this issue. The hybrid

radio-over-fiber system has been studied many years as a promising approach to provide the wireless broadband service [2]-[4]. The advantage of the radio-over-fiber system is that the signal generation and signal processing are centralized in the central station (CS) before transporting via the fiber to a number of the remote base stations (BSs). Such architecture can make the CS more complicated and allow the BSs share resources, thereby simplifying the architecture of the BS. The increasing number of the remote BSs with small millimetre-wave band coverage such as pico-cell requires the implementation of the simple and compact BS in term of the cost. Therefore, many techniques have been studied in order to explore the cost-effective radio-over-fiber system. In [4]-[6], the light source sharing technique is proposed, thereby requiring no lasers installed in the BS in order to make the BS passive [7].

However, the performance of the radio-over-fiber system may be degraded by the fiber chromatic dispersion. As a solution to overcome this effect, the single sideband subcarrier modulation technique [8] as a solution is proposed, which modulate the optical carrier with either the lower sideband (LSB) or upper sideband (USB) subcarrier. Moreover, the optical external modulators, such as the intensity modulator of either the MZ modulator or the EA modulator is the preferred choice to generate the sideband subcarrier signal to overcome the effect of laser frequency chirps suffered by the direct modulation technique. More importantly, the EA modulator can be a promising choice in the future to design the maintenance-free BS in which no power supply is required [7].

Due to the architecture characteristic of the millimetre-wave band system, a larger number of the BSs are connected to the CS via ROF networks. As such, the dense wavelength division multiplexing technique is a strong candidate to support the simultaneous BS connection to the CS. Many reports [2]-[3], [9] have proposed the solution to address the issue. In [2], the DWDM spectrum scheme by using frequency-interleaving technique is introduced. In order to demultiplex the DWDM signal at CS, the dual mode remote light is designed at CS. This technique is possible to use for uplink data transmission but it is not a good choice for downlink data transmission because it increase the complexity of architecture of BS, which conflicts the objective to design the simple BS. In addition, the mode interval of the dual-mode local light has to be tuned accurately in order to ensure the local light beat with the desired optical carrier and corresponding subcarrier. So the drawback is that the tight restriction is imposed on either the wavelength allocation of optical carrier and corresponding subcarrier or the mode interval of the dual-mode light. As another solution to process the DWDM spectrum generated by using the optical frequency interleaving technique, the photonic downconversion (PDC) technique [9] is developed. The MZ modulator acting as a generator of carrier-suppressed DSB is used at CS to complete the downshift and up-shift function in order to process the DWDM spectrum. However, the same drawback as [2] is that the PDC is suitable for uplink data transmission but it is not a good choice for downlink data transmission. As a result, the new approach with the DWDM of 25 GHz spacing proposed in this thesis is designed to overcome the drawbacks mentioned above. Simply, the square-law detection of photodiode is utilized to generate the desired 60 GHz RF signal without using either PDC technique or the dual-mode light at CS. In [3], the

wavelength interleaving technique for WDM ROF system is proposed in order to increase the capacity and improve the spectral efficiency. However, the wavelength interleaving multiplexer and demultiplexer have to be designed. In our approach, DWDM spectrum with 25 GHz spacing is not the frequency interleaving technique. Therefore, the existing DWDM multiplexer and demultiplexer are adopted in the demonstrated system. Moreover, the 60 GHz signal can be generated from the lower RF frequency, i.e. 10 GHz. Usually, the implementation of DWDM with the involvement of single sideband transmission in the mm-wave band results in the poor optical spectral efficiency because the typical WDM channel spacing is more than 50 GHz. In [10], the wavelength interleaving approach is proposed to improve the spectral efficiency but the channel spacing has to be 83.6 GHz, which does not achieve the better spectral efficiency.

In general, with consideration of the above drawbacks, the DWDM with 25 GHz spacing in this thesis is implemented at CS to improve the spectral efficiency. In addition, the light sharing technique is adopted at BS to share the laser at CS, thereby simplifying the architecture of BS.

The demonstrated system is based on the star-tree architecture incorporating the external modulation. The optical bandpass filter in the BS as a channel selection scheme is designed to select the desired optical carriers and corresponding subcarriers in order to generate the 60 GHz signal. By making use of the mature electrical signal processing technology, the direct detection technique is adopted at BS to detect the DPSK modulated signal. In order to prove the concept, the demonstrated system is set up with 1 CS and 3

BSs and the 155Mbps data transmits via the 25 km no-amplifying single mode fiber link on the downlink and uplink direction simultaneously.

As a wireless access system, the transmission distance of ROF system is about 25 km or 50 km, much shorter than the distance of long-haul optical transmission system. As a result, the optical power launched into the fiber is very low, 0.5mw in the demonstrated system. So the non-linearity effect, which has to be taken into account when designing the long-haul optical transmission system, is not a contributing factor to degrade the system performance.

The thesis is organized with the following structure to describe the demonstrated system. Chapter 2 provides the description of system principle with mathematical expression and illustrates the channel allocation of the DWDM spectrum. Chapter 3 describes the simulation setting-up with key parameters and the simulation results while chapter 4 discusses the system performance degradation by the bandwidth of the electrical filters or the limitation by the laser phase noise. Finally, the conclusions are present in chapter 5.

# Chapter 2 System Description

## 2.1 Network architecture

The DWDM ROF system network architecture has many various network topologies such as star-tree, ring or bus topology. However, the star-tree architecture as shown in Fig. 2.1 is considered here as an example.

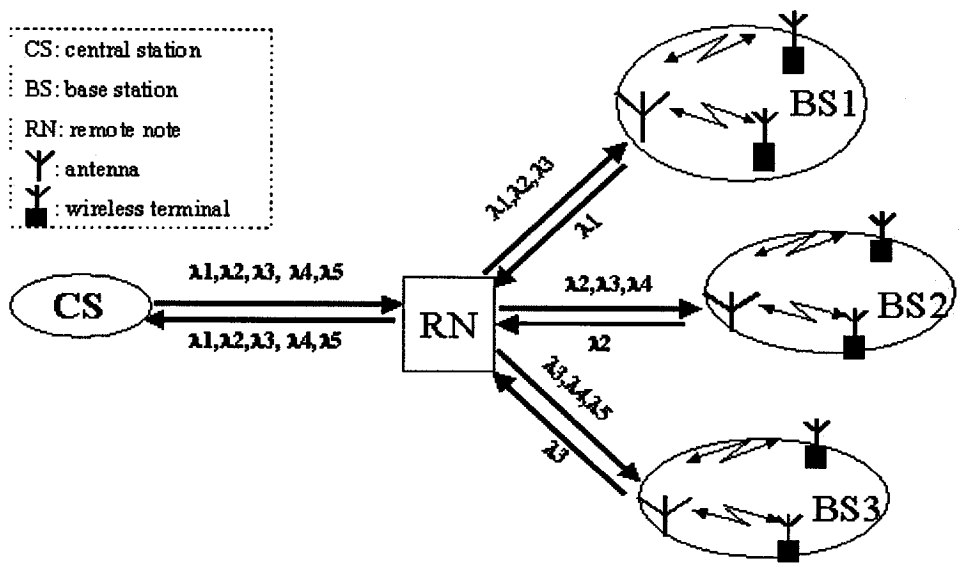


Figure 2.1 DWDM star tree network architecture

A key to the DWDM access is to use the wavelength for the connection between the CS and BSs. Assume the star is consist of two unilateral fiber links. Three wavelengths ($\lambda_i$ $\lambda_{i+1}$ $\lambda_{i+2}$ ), (i=1,....., N) are assigned to the downlink (CS to BSi) connections and the wavelength ($\lambda_i$) is assigned to the uplink (BSi to CS) connection. The downlink system configuration is illustrated in Fig. 2.2.

In Fig.2.2, the 5 optical channels are transmitted. Each channel consists of a CW laser source, a MZ modulator, two DPSK modulators at the downlink RF output of $f_d$ and two PRBS $2^{23}$-1 data source except that the first channel at wavelength $\lambda_1$ has only a laser without carrying any subcarriers. In each channel, an optical carrier or wavelength carries two sideband RF subcarriers containing different data. DWDM multiplexes 5 channels and corresponding subcarriers together and sends to the BSs via the 25 km downlink SMF link. At the base station, every 3 adjacent channels at the wavelengths ($\lambda_i$ $\lambda_{i+1}$ $\lambda_{i+2}$) are selected by an optical bandpass filter. In order to share a light source from the CS, a 90/10-power splitter after the optical bandpass filter splits the optical power into two parts, 90% of which is reserved for uplink transmission and 10% of which is pass to a photodiode for photodetection. An electrical bandpass filter is designed to eliminate the unwanted beating signals and extract 60 GHz signal for DPSK demodulator to recover the downlink data.

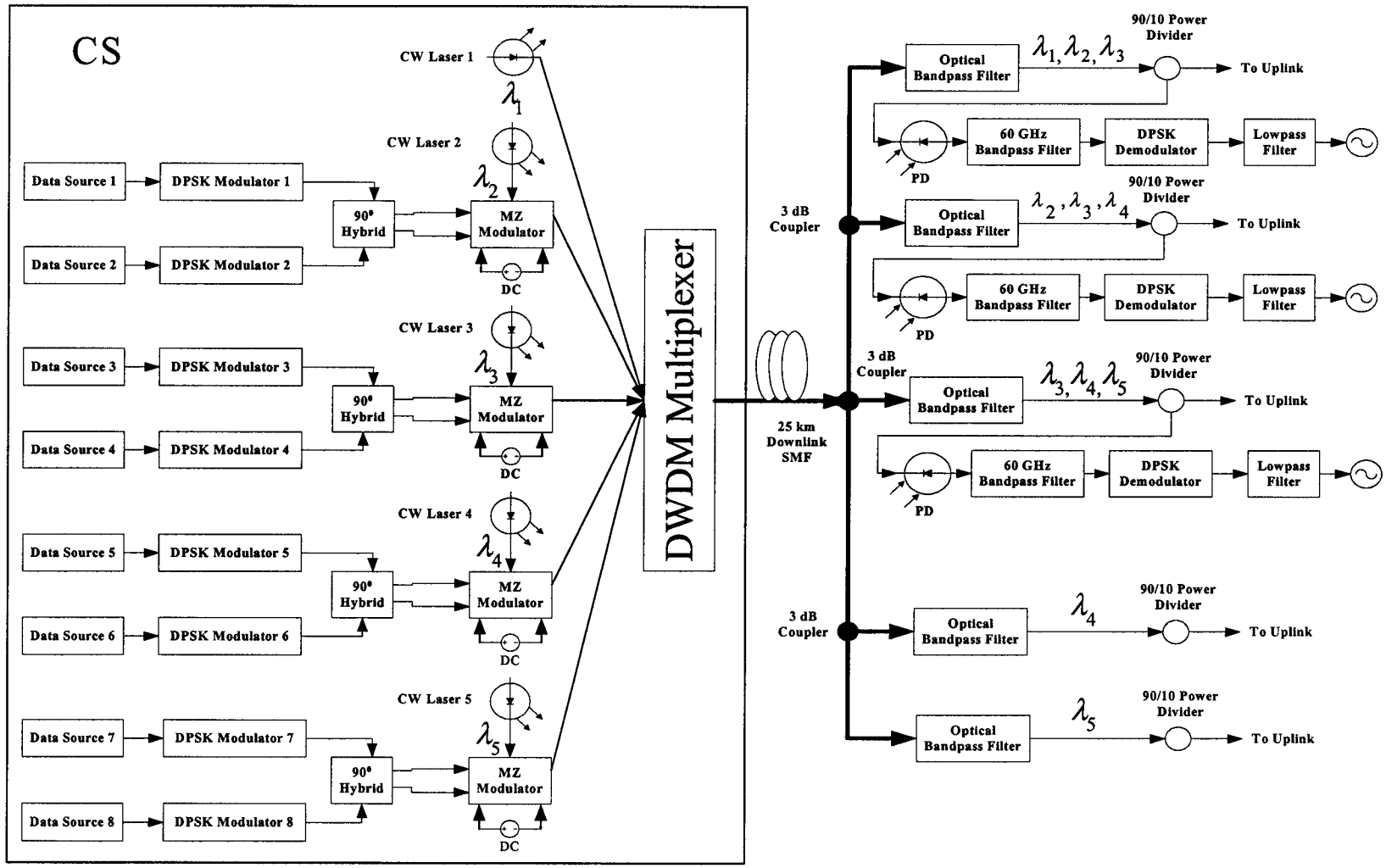


Figure 2.2 Downlink system configuration

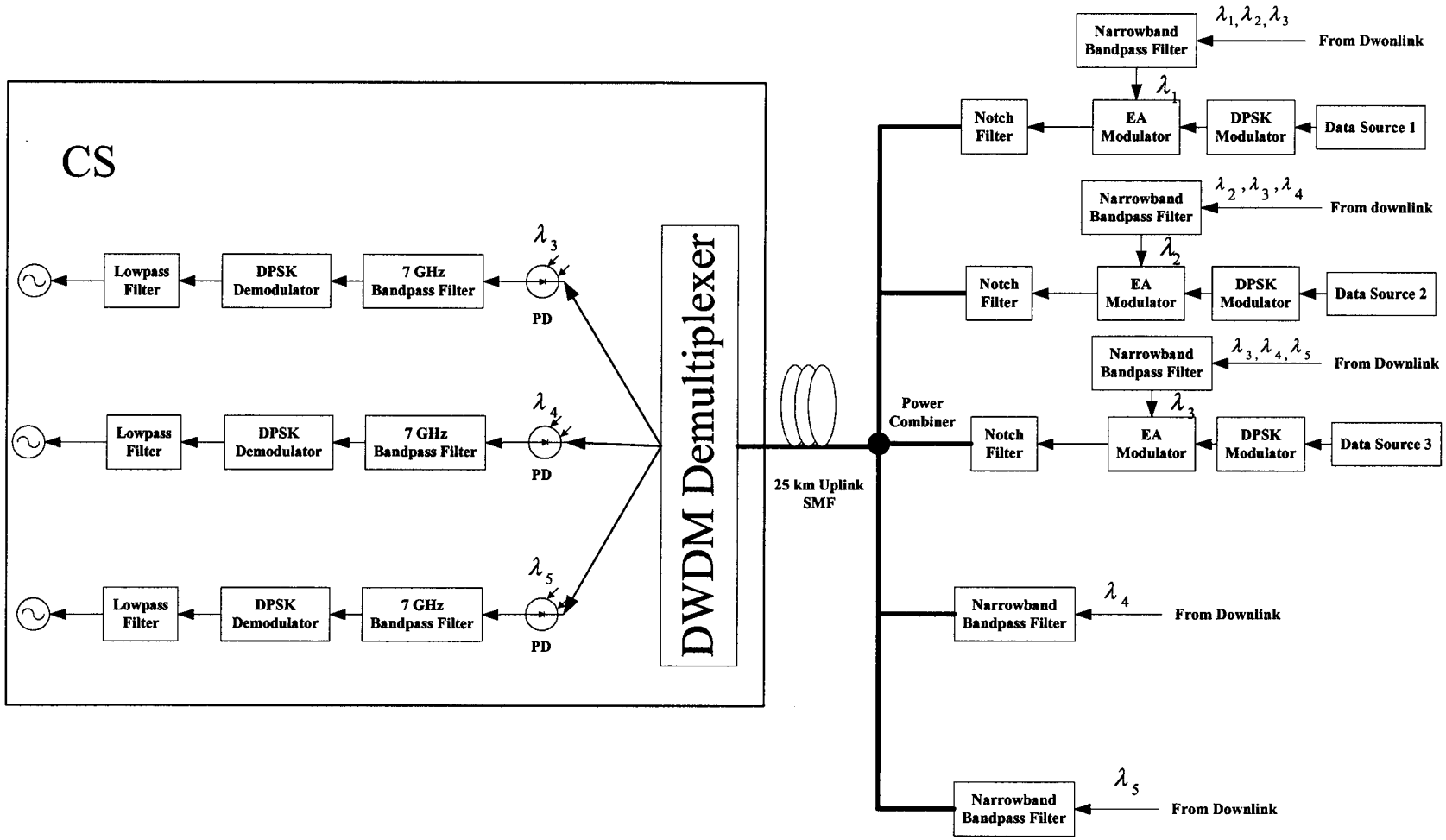


Figure 2.3 Uplink system configuration

In the uplink direction, the base station is designed without local laser. An optical narrowband bandpass filter selects the first channel at the wavelength $\lambda_i$ of every three adjacent channels coming from the central station tapped by a 90/10 power splitter. The EA modulator utilizes the remote light at the wavelength $\lambda_i$ to modulate the RF subcarrier at the uplink frequency $f_u$ on the optical carrier. In order to overcome the fiber dispersion effect, a notch filter [11] eliminates the USB subcarrier so as to generate the single sideband (SSB) spectrum. The optical combiners combine all the uplink SSB signals from each BS and send to the central station via the 25 km uplink fiber. Then, the DWDM demultiplexer with channel spacing of 25 GHz at the CS demultiplexes each individual optical channel and corresponding RF subcarrier, which is detected by a photodiode. An electrical bandpass filter is adopted to select the 7 GHz signal for DPSK demodulator to recover the uplink data.

## 2.2 The Principle of Downlink Spectrum

### 2.2.1 DSB Generation Containing Two Sets of Data

In order to have better spectral efficiency, the double sideband (DSB) subcarrier with different data is used. In other words, the lower sideband and upper sideband signals simultaneously locate on the both side of the optical carrier but the LSB and USB subcarriers contain different data. Figure 2.4 illustrates the optical spectrum in DSB format which outputs from the external modulator such as MZ modulator, where $C_n$ represents the *nth* channel of the optical carrier at frequency $f_{cn} = c/\lambda_{cn}$, $c$ is the

light speed in the vacuum and $\lambda_{cn}$ is the wavelength of the optical carrier $C_n$; $U_n$ and $L_n$ represent the upper sideband subcarrier at frequency $f_{cn}+f_d$ and lower sideband subcarrier at frequency $f_{cn}-f_d$, $f_d$ is the radio frequency of electrical modulator; $n=1,2,3,.....N$ represents the number of the optical channel.

Because the channel spacing in DWDM is 25 GHz, the maximum distance between LSB and USB is 25 GHz. Therefore, $f_d$ is chosen to be within the maximum distance.

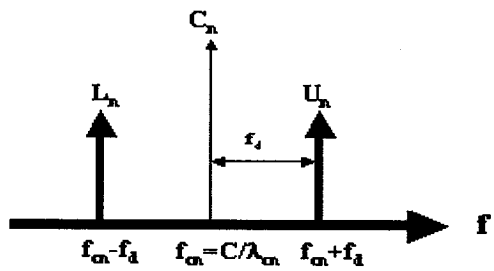


Figure 2.4 Spectra from an optical modulator

However, the maximum could be different with the different channel spacing in DWDM. More importantly, the LSB and USB subcarriers contain different data information.

### 2.2.2 DWDM Downlink Spectrum

The DWDM multiplexer is to multiplex all the output from the optical external modulator together. Figure 2.5 (a) illustrates the spectrum output from DWDM. The channel spacing in DWDM is 25 GHz and each optical channel carries the DSB

subcarrier. As an example, the 5 channels are shown in the figure. This is the spectrum to be transmitted via the downlink fibre to the base station.

After the DWDM signal arrives at the *nth* base station, the optical bandpass filter is utilized to choose which optical carrier and subcarriers are used for photodetection. Because the 60 GHz ROF system is designed, the optical carriers and subcarriers are chosen to have 60 GHz signal generated. As a result, three adjacent optical channels as shown in Figure 2.5 (a) are filtered out by an optical bandpass filter and then applied to a photodiode. The bandwidth of filter has to cover the first optical carrier and the LSB subcarrier of the third optical channel. As illustrated in the Figure 2.5 (b), if the reference wavelength for a photodiode is the wavelength of the optical channel $C_n$, the channels $C_n$, $C_{n+1}$, $C_{n+2}$ and subcarriers $L_n$, $U_{n+1}$, $L_{n+1}$, $U_{n+2}$, $L_{n+2}$ are chosen as three adjacent channels. As an example, the radio frequency $f_{dn}$ of subcarriers is 10 GHz and the channel spacing $f_{ch}$ is 25 GHz, so the 60 GHz signal is generated after beating between the optical carrier $C_n$ and the subcarrier $L_{n+2}$.

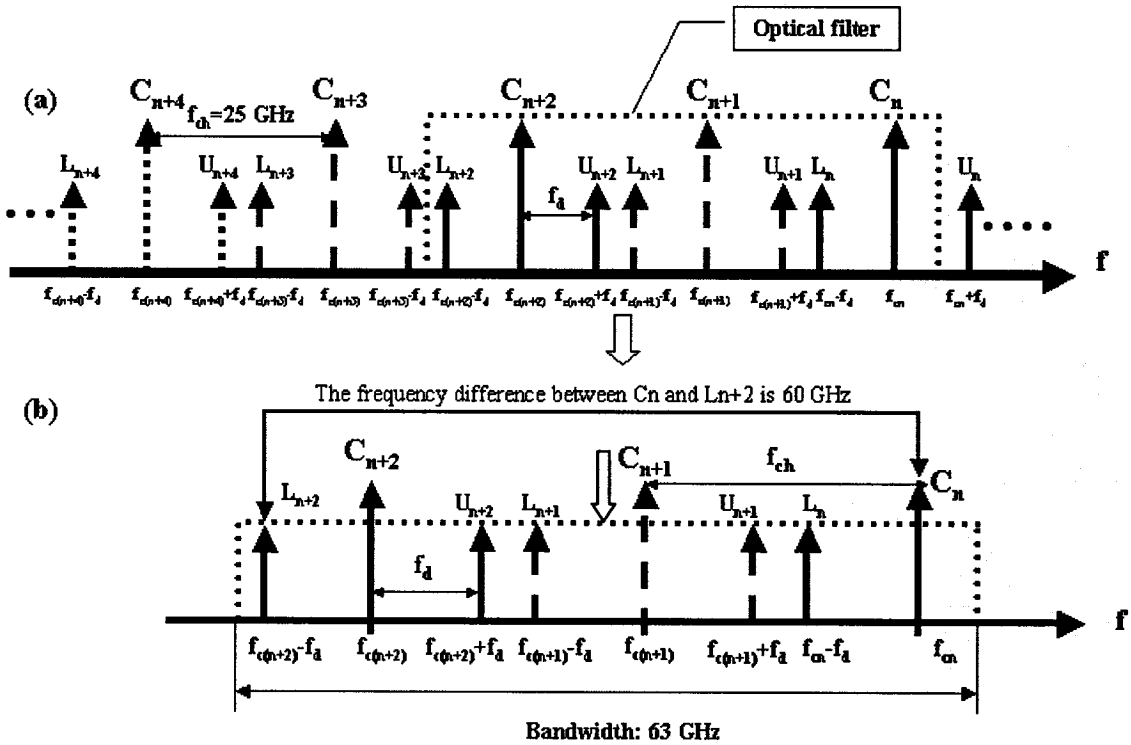


Figure 2.5 (a) DWDM output signal; (b) Three adjacent channels and subcarriers for generating the 60 GHz signal

### 2.2.3 Mathematical Explanation for The Downlink Spectrum

The complex electric field of an optical carrier $C_n$ [5] is usually expressed by

$$e_{cn}(t) \propto \sqrt{2P_{cn}} \exp\{j\varphi_{cn}(t)\} \tag{1}$$

$$\varphi_{cn}(t) = 2\pi f_{cn} t + \phi_{cn}(t) \tag{2}$$

where $P_{cn}$, $f_{cn}$, and $\phi_{cn}(t)$ are the constant power, carrier frequency and phase noise of single mode light source $C_n$, respectively.

The USB RF downlink signal is expressed by

$$m_{dn}(t) = V_{dn} \cdot \exp\{j\varphi_{dn}(t)\} \tag{3}$$

$$\varphi_{dn}(t) = 2\pi f_{dn} t + \theta_{dn}(t) \tag{4}$$

The LSB RF downlink signal is expressed by

$$m'_{dn}(t) = V_{dn} \cdot \exp\{j\varphi'_{dn}(t)\} \tag{5}$$

$$\varphi'_{dn}(t) = 2\pi f_{dn} t + \theta'_{dn}(t) \tag{6}$$

where $V_{dn}$ and $f_{dn}$ are the amplitude and carrier frequency of RF downlink signal; $\theta_{dn}(t)$ and $\theta'_{dn}(t)$ are the payload data of RF USB and LSB downlink signal, respectively.

In order to generate optical single sideband (OSSB) signal, the dual arm MZ modulator ([12], [13]) is used with the DC bias at the quadrature point. If the same RF USB signal $m_{dn}(t)$ with a phase difference of $\frac{\pi}{2}$ drives on the two arms, the output complex optical field is written as [8]

$$\begin{aligned} E_{cn1} = \frac{\sqrt{2P_{cn}}}{2}\{&\cos\left[2\pi f_{cn} t + \phi_{cn}(t) + \frac{\pi}{2} + \beta\pi\cos[2\pi f_{dn} t + \theta_{dn}(t)]\right] \\ &+ \cos\left[2\pi f_{cn} t + \phi_{cn}(t) + \beta\pi\cos\left(2\pi f_{dn} t + \theta_{dn}(t) + \frac{\pi}{2}\right)\right]\} \\ = \frac{\sqrt{2P_{cn}}}{2}\{&\sqrt{2}J_0(\beta\pi)\sin[2\pi f_{cn} t + \phi_{cn}(t) - \frac{\pi}{4}] \\ &- 2J_1(\beta\pi)\cos[2\pi(f_{cn} + f_{dn})t + \phi_{cn}(t) + \theta_{dn}(t)] \\ &+ .....\} \end{aligned} \tag{7}$$

If the same RF LSB signal $m_{dn}^{'}(t)$ with a phase difference of $(-\frac{\pi}{2})$ drives on two arms, the output complex optical field is written as

$$E_{cn2} = \frac{\sqrt{2P_{cn}}}{2}\{\cos\left[2\pi f_{cn}t + \phi_{cn}(t) + \frac{\pi}{2} + \beta\pi\cos[2\pi f_{dn}t + \theta_{dn}(t)]\right] \tag{8}$$

$$+\cos\left[2\pi f_{cn}t + \phi_{cn}(t) + \beta\pi\cos\left(2\pi f_{dn}t + \theta_{dn}(t) - \frac{\pi}{2}\right)\right]\}$$

$$= \frac{\sqrt{2P_{cn}}}{2}\{\sqrt{2}J_0(\beta\pi)\sin[2\pi f_{cn}t + \phi_{cn}(t) - \frac{\pi}{4}]$$

$$-2J_1(\beta\pi)\cos[2\pi(f_{cn} - f_{dn})t + \phi_{cn}(t) - \theta_{dn}(t)]$$

$$+.....\}$$

where $J_0$ and $J_1$ are the zeroth and first-order terms of Bessel function, respectively; $\beta\pi = \pi V_{ac}/V_{\pi}$ is the normalized amplitude of the RF drive signal. $V_{\pi}$ is the switching voltage of MZ modulator and $V_{ac}$ is the amplitude of RF Signal.

If the USB signal $m_{dn}(t)$ and LSB signal $m_{dn}^{'}(t)$ are simultaneously applied on both arms of MZ modulator, the complex field of modulator output is expressed by

$$E_{cn}^{out} = E_{cn1} + E_{cn2} \tag{9}$$

Hence, the upper sideband subcarrier $U_n$ at $f_{cn} + f_{dn}$ and the lower sideband subcarrier $L_n$ at $f_{cn} - f_{dn}$ are modulated beside the optical carrier $C_n$ as shown in Figure

2.4. In reality, modulation depth $\beta\pi << 1$ is maintained so that the second or higher harmonics are neglected.

The similar expression can be deduced for the optical carriers $C_{n+1}$ and $C_{n+2}$. In order to describe how the 60 GHz signal is generated, only the expression of LSB subcarrier $L_{n+2}$ is given here.

The complex electric field of an optical carrier $C_{n+2}$ is usually expressed by [5]

$$e_{c(n+2)}(t) \propto \sqrt{2P_{c(n+2)}} \exp\{j\varphi_{c(n+2)}(t)\} \tag{10}$$

$$\varphi_{c(n+2)}(t) = 2\pi f_{c(n+2)} t + \phi_{c(n+2)}(t) \tag{11}$$

where $P_{c(n+2)}$, $f_{c(n+2)}$, and $\phi_{c(n+2)}(t)$ are the constant power, carrier frequency and phase noise of single mode light source $C_{n+2}$, respectively.

The USB RF downlink signal is expressed by

$$m_{d(n+2)}(t) = V_{d(n+2)} \cdot \exp\{j\varphi_{d(n+2)}(t)\} \tag{12}$$

$$\varphi_{d(n+2)}(t) = 2\pi f_{d(n+2)} t + \theta_{d(n+2)}(t) \tag{13}$$

The RF LSB signal is expressed by

$$m'_{d(n+2)}(t) = V_{d(n+2)} \cdot \exp\{j\varphi'_{d(n+2)}(t)\} \tag{14}$$

$$\varphi'_{d(n+2)}(t) = 2\pi f_{d(n+2)} t + \theta'_{d(n+2)}(t) \tag{15}$$

where $V_{d(n+2)}$ and $f_{d(n+2)}$ are the amplitude and carrier frequency of RF downlink signal in the (n+2)th optical channel ; $\theta_{d(n+2)}(t)$ and $\theta'_{d(n+2)}(t)$ are the payload data of RF USB and LSB downlink signal, respectively.

Then, the optical field of LSB subcarrier $L_{n+2}$ can be approximately expressed by

$$E_{c(n+2)}^{LSB} = -\sqrt{2P_{c(n+2)}}J_1(\beta\pi)\cos[2\pi(f_{c(n+2)} - f_{d(n+2)})t + \phi_{c(n+2)}(t) - \theta_{d(n+2)}(t)] \quad (16)$$

Therefore, after a DWDM multiplexes three optical carriers $C_n, C_{n+1}, C_{n+2}$ and corresponding subcarrier $U_n, L_n, U_{n+1}, L_{n+1}, U_{n+2}, L_{n+2}$, the optical field of DWDM is given by

$$E_{DWDM}^{out} = E_{cn}^{out} + E_{c(n+1)}^{out} + E_{c(n+2)}^{out} \quad (17)$$

After transmitting over the downlink fiber with the length of $X_d$ and the propagation constant of $\beta_{d,n}(f)$, the optical signal is split by a 90/10-power divider. The 10% of power is sent to a photodiode to recover the downlink data in the BS, and the 90% of power is used as a light source for uplink transmission. The propagation constant $\beta_{d,n}(f)$ is approximated as [14]

$$\beta_{d,n}(f) \approx \beta_{d0,n} + \beta_{d1,n} \cdot 2\pi(f - f_{cn}) + \frac{1}{2}\beta_{d2,n} \cdot \{2\pi(f - f_{cn})\}^2 \quad (18)$$

Here, $\beta_{d1,n}X_d$ corresponds to the group-delay time, and $\beta_{d2,n}$ is related with the downlink fiber dispersion parameter $D_{d,n}$ as

$$\beta_{d2.n} = \frac{\lambda_{cn}^2}{2\pi c} \cdot D_{d,n} \tag{19}$$

Hence, the former part $E_{DWDM}^{downlink}$ and latter part $E_{DWDM}^{uplink}$ of optical field after propagating over the downlink fiber are written as [5]

$$E_{DWDM}^{downlink} = \sqrt{a_{opd}} \times E_{DWDM}^{'out} \tag{20}$$

$$\propto \sqrt{a_{opd}} \times (E_{cn}^{'out} + E_{c(n+1)}^{'out} + E_{c(n+2)}^{'out})$$

$$\propto \sqrt{a_{opd}} \times \{\sqrt{2P_{cn}} \{\sqrt{2} J_0(\beta\pi) \sin[\psi_{0,n}(t, X_d) - \frac{\pi}{4}]$$

$$-J_1(\beta\pi)\cos[\psi_{1,n}(t, X_d)] - J_1(\beta\pi)\cos[\psi_{-1,n}(t, X_d)]\}$$

$$+ \{\sqrt{2P_{c(n+1)}} \{\sqrt{2} J_0(\beta\pi) \sin[\psi_{0,(n+1)}(t, X_d) - \frac{\pi}{4}]$$

$$-J_1(\beta\pi)\cos[\psi_{1,(n+1)}(t, X_d)] - J_1(\beta\pi)\cos[\psi_{-1,(n+1)}(t, X_d)]\}$$

$$+ \{\sqrt{2P_{c(n+2)}} \{\sqrt{2} J_0(\beta\pi) \sin[\psi_{0,(n+2)}(t, X_d) - \frac{\pi}{4}]$$

$$-J_1(\beta\pi)\cos[\psi_{1,(n+2)}(t, X_d)] - J_1(\beta\pi)\cos[\psi_{-1,(n+2)}(t, X_d)]\}$$

$$\}$$

$$E_{DWDM}^{uplink} = \sqrt{1 - a_{opd}} \times E_{DWDM}^{'out}$$

$$\propto \sqrt{1 - a_{opd}} \times (E_{cn}^{'out} + E_{c(n+1)}^{'out} + E_{c(n+2)}^{'out})$$

$$\propto \sqrt{1 - a_{opd}} \times \{\sqrt{2P_{cn}} \{\sqrt{2} J_0(\beta\pi) \sin[\psi_{0,n}(t, X_d) - \frac{\pi}{4}]$$

$$-J_1(\beta\pi)\cos[\psi_{1,n}(t, X_d)] - J_1(\beta\pi)\cos[\psi_{-1,n}(t, X_d)]\}$$

$$+ \{\sqrt{2P_{c(n+1)}} \{\sqrt{2} J_0(\beta\pi) \sin[\psi_{0,(n+1)}(t, X_d) - \frac{\pi}{4}]$$

$$-J_1(\beta\pi)\cos[\psi_{1,(n+1)}(t,X_d)]-J_1(\beta\pi)\cos[\psi_{-1,(n+1)}(t,X_d)]\}$$

$$+\{\sqrt{2P_{c(n+2)}}\{\sqrt{2}J_0(\beta\pi)\sin[\psi_{0,(n+2)}(t,X_d)-\frac{\pi}{4}]$$

$$-J_1(\beta\pi)\cos[\psi_{1,(n+2)}(t,X_d)]-J_1(\beta\pi)\cos[\psi_{-1,(n+2)}(t,X_d)]\}$$

$$\} \tag{21}$$

where $\psi_{p,n}(t,X_d)$ is defined as

$$\psi_{p,n}(t,X_d)=\varphi_{cn}(t)+p\varphi_{dn}(t)-\beta_{d,n}(f)\cdot X_d$$

$$\approx 2\pi(f_{cn}+pf_{dn})(t-\beta_{d1,n}X_d)$$

$$+\phi_{cn}(t-\beta_{d1,n}X_d)+p\theta_{dn}(t-\beta_{d1,n}X_d)$$

$$-\frac{1}{2}\beta_{d2,n}\cdot\{2\pi(pf_d)\}^2\cdot X_d-(\beta_{d0.n}-\beta_{d1,n}\cdot 2\pi f_{cn})\cdot X_d \tag{22}$$

Here, $a_{opt}$ is the bifurcation ratio of the optical power divider.

By using the square law detection of a photodiode with reference wavelength $\lambda_{cn}$ on the optical carrier $C_n$ in the BS, seven spectra are generated from the optical signal $E_{DWDM}^{downlink}$, but the interesting photocurrent, resulting from beating between the optical carrier $C_n$ and the LSB subcarrier $L_{n+2}$, is given by

$$i_{cn,L(n+2)}(t,X_d)\propto 2Ra_{opt}\sqrt{2P_{cn}P_{c(n+2)}}J_0(\beta\pi)J_1(\beta\pi)\sin[\psi_{cn,L(n+2)}(t,X_d)] \tag{23}$$

where R is the responsivity of a photodiode and then $\psi_{cn,L(n+2)}(t,X_d)$ is defined as

$$\psi_{cn,L(n+2)}(t,X_d)=\psi_{0,n}(t,X_d)-\psi_{-1,n+2}(t,X_d)$$

$$=2\pi(f_{cn}-f_{c(n+2)}+f_{d(n+2)})(t-\beta_{d1,n}X_d)$$

$$+\phi_{cn}(t-\beta_{d1,n}X_d)-\phi_{c(n+2)}(t-\beta_{d1,n+2}X_d)+\theta_{d(n+2)}(t-\beta_{d1,n+2}X_d)$$

$$+\frac{1}{2}\beta_{d2,n+2}\cdot(2\pi f_{d(n+2)})^2 X_d$$

$$+[\beta_{d1,n}\cdot 2\pi(f_{cn}-f_{c(n+2)})\cdot X_d]-\frac{\pi}{4} \qquad (24)$$

Here, it is neglected that the propagation constant $\beta_{d,n}(t)$ is varied with different wavelength of optical carriers. In this case, the frequency difference $f_{cn}-f_{c(n+2)}$ is 50 GHz. If radio frequency $f_{d(n+2)}$ is chosen as 10 GHz, as a result, the frequency of beating signal between the optical carrier $C_n$ and the LSB subcarrier $L_{n+2}$ is 60 GHz. The desired RF downlink signal $i_{cn,L(n+2)}(t,X_d)$ is selected by an electrical bandpass filter with central frequency of $f_{cn}-f_{c(n+2)}+f_{d(n+2)}$ and propagated via a millimeter-wave antenna to a terminal. If the payload data $\theta_{d(n+2)}(t)$ is differentially encoded, i.e. DPSK modulated in the demonstrated system, the RF down photocurrent $i_{cn,L(n+2)}(t,X_d)$ can be decoded by the differential detection scheme without any serous dispersion degradation.

However, as noted in eq.(24), the laser phase noise term $\phi_{cn}(t)-\phi_{c(n+2)}(t)$ cannot be cancelled because $\phi_{cn}(t)$ and $\phi_{c(n+2)}(t)$ originate from two different light sources. As a result, this is a limiting factor on the system performance. In order to investigate the extent of laser phase noise effect, the simulation is performed in two different cases: the ideal case [$\phi_{cn}(t)-\phi_{c(n+2)}(t)=0$] and the actual case [$\phi_{cn}(t)-\phi_{c(n+2)}(t)\neq 0$].

In addition, the USB subcarrier $U_n$ of optical carrier $C_n$ is not included in the bandwidth of an optical bandpass filter. If $U_n$ is included in the optical signal for photodetection, the photocurrent $i_{c(n+2),Un}(t, X_d)$, generated by beating between the optical carrier $C_{n+2}$ and subcarrier $U_n$, is expressed by

$$i_{c(n+2),Un}(t, X_d) \propto 2Ra_{opt}\sqrt{2P_{cn}P_{c(n+2)}}J_0(\beta\pi)J_1(\beta\pi)\sin[\psi_{c(n+2),Un}(t, X_d)] \tag{25}$$

where $\psi_{c(n+2),Un}(t, X_d)$ is given by

$$\begin{aligned}\psi_{c(n+2),Un}(t, X_d) &= \psi_{0,n+2}(t, X_d) - \psi_{1,n}(t, X_d) \\ &= 2\pi(f_{cn} - f_{c(n+2)} + f_{dn})(t - \beta_{d1,n}X_d) \\ &\quad + \phi_{cn}(t - \beta_{d1,n}X_d) - \phi_{c(n+2)}(t - \beta_{d1,n+2}X_d) + \theta_{dn}(t - \beta_{d1,n}X_d) \\ &\quad - \frac{1}{2}\beta_{d2,n}\cdot(2\pi f_{dn})^2 X_d \\ &\quad - [\beta_{d1,n}\cdot 2\pi(f_{cn} - f_{c(n+2)})\cdot X_d] + \frac{\pi}{4}\end{aligned} \tag{26}$$

Assuming the variation of propagation constant $\beta_{d2,n}$ and $\beta_{d2,n+2}$ with the wavelength is neglected and $f_{d(n+2)} = f_{dn}$, the frequency component $f_{cn} - f_{c(n+2)} + f_{dn}$ is same as one in the photocurrent $i_{cn,L(n+2)}(t, X_d)$. But the two payload data are different. As a result, this causes the crosstalk at the frequency $f_{cn} - f_{c(n+2)} + f_{d(n+2)}$. If the phase difference is $\pi$, the phase component is cancelled and the payload data cannot be decoded correctly. Therefore, the subcarrier $U_n$ has to be ruled out.

## 2.3 The principle of Uplink Spectrum

### 2.3.1 Remote Light Source

One of challenge to design radio-over-fibre access system is to simplify the architecture of the base station. Many approaches have been investigated [5], [15]-[16]. An approach used in here is to share the light source coming from the central station, which is similar configuration as shown in [5]. As illustrated in Figure 2.4, the three adjacent channels are filtered out for the *nth* base station. The fraction of the downlink optical signal $E_{DWDM}^{uplink}$ in eq.(21), which is filtered out by an optical bandpass filter at central wavelength $\lambda_{cn}$ of optical carrier $C_n$, is used as a local light to modulate the RF uplink signal $m_{un}(t)$ by an EA modulator for uplink transmission in the *nth* base station.

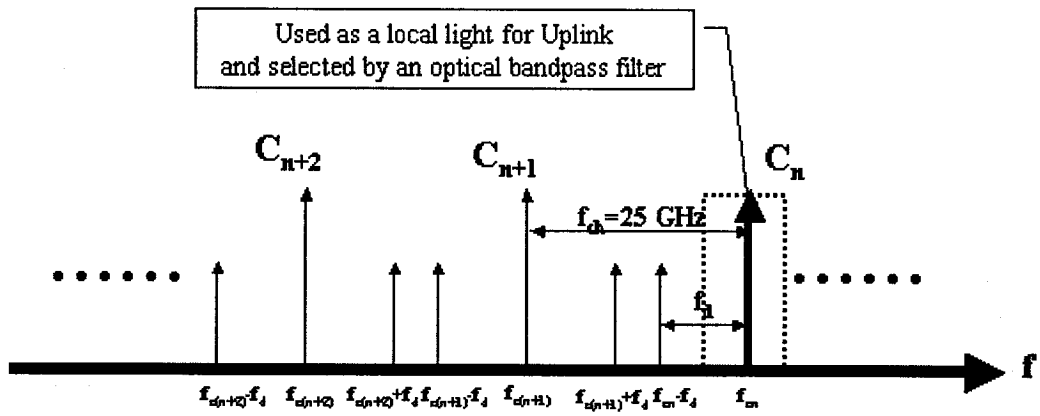


Figure 2.6 Spectrum after an optical bandpass filter on the downlink for three adjacent channels $C_n$, $C_{n+1}$ and $C_{n+2}$; $C_n$ is filtered out by an optical bandpass filter and used as a local light source for uplink transmission

After the downlink optical signal $E_{DWDM}^{uplink}$ passes the optical bandpass filter at central wavelength $\lambda_{cn}$ of optical carrier $C_n$, the filtered-out optical carrier $C_n$ can be approximately expressed by

$$E_{cn}^{uplink} \propto 2\sqrt{(1-a_{opd})P_{cn}}J_0(\beta\pi)e^{j\left(\psi_{0,n}(t,X_d)-\frac{\pi}{4}\right)} \tag{27}$$

The RF uplink signal $m_{un}(t)$ is expressed by

$$m_{un}(t) = V_{un}\exp\{j\varphi_{un}(t)\} \tag{28}$$

$$\varphi_{un}(t) = 2\pi f_{un}t + \theta_{un}(t) \tag{29}$$

where $V_{un}$, $f_{un}$ and $\theta_{un}(t)$ are the amplitude, the carrier frequency, and the payload data of the RF uplink signal as to the optical carrier $C_n$, respectively.

Hence, the complex electric field of the modulated optical signal $E_{un}(t, X_d)$ is then written by [5]

$$\begin{aligned} E_{un}(t,X_d) &= M_B[m_{un}(t)]\cdot E_{cn}^{uplink} \\ &\propto 2\sqrt{(1-a_{opd})P_{cn}}J_0(\beta\pi)\times\{b_{-1}e^{j\left(\psi_{0,n}(t,X_d)-\phi_{un}(t)-\frac{\pi}{4}\right)} \\ &\quad + b_0 e^{j(\psi_{0,n}(t,X_d)-\frac{\pi}{4})} \\ &\quad + b_1 e^{j\left(\psi_{0,n}(t,X_d)+\phi_{un}(t)-\frac{\pi}{4}\right)}\} \\ &\quad n = 1,2,.....n,n+1,n+2,.....N \end{aligned} \tag{30}$$

where $M_B[m_u(t)]$ is the transfer function of modulator and depends on the modulation scheme as well. $b_r(r=-\infty,+\infty)$ is the Fourier coefficient as a function of $V_{un}$. In order to avoid the fiber chromatic dispersion [15] as usually caused by the DSB signal, the notch filer is adopted to eliminate the USB signal $f_{cn}+f_{un}$ and to keep LSB signal $f_{cn}-f_{un}$ as

shown in Figure 2.7 at the optical carrier $C_n$ with wavelength $\lambda_{cn}$, where $L_n$ represents the LSB signal and $f_{un}$ is the RF uplink frequency defined as 57 GHz in the system.

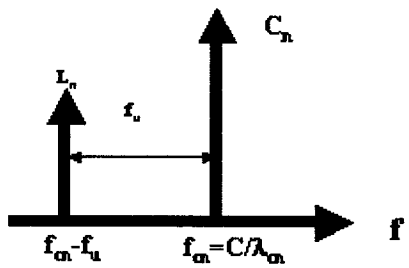


Figure 2.7 Uplink spectra of the optical channel $C_n$

Hence, the optical field of the uplink signal after the notch filter is expressed by

$$E_{un,LSB}(t,X_d) \propto 2\sqrt{(1-a_{opd})P_{cn}}J_0(\beta\pi)\times\{b_{-1}e^{j\left(\psi_{0,n}(t,X_d)-\phi_{un}(t)-\frac{\pi}{4}\right)}$$

$$+b_0 e^{j(\psi_{0,n}(t,X_d)-\frac{\pi}{4})}\} \qquad (31)$$

### 2.3.2 Uplink Spectrum for DWDM Demultiplexing

The modulated optical signal of each BS is combined by an optical combiner at one remote node of star-tree structure to generate the uplink spectra as shown in Figure 2.8(a).

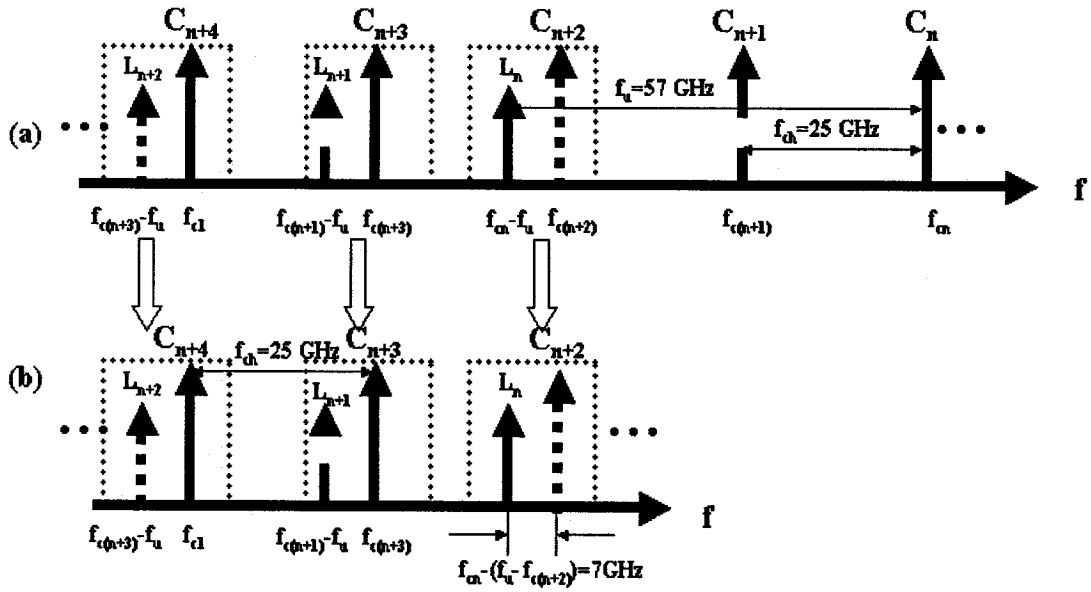


Figure 2.8 (a) Uplink spectrum; (b) New DWDM channels for DWDM demultiplexer at the central station

Therefore, the combined optical signal can be expressed by

$$E_{combined,LSB}(t,X_d)=E_{un,LSB}(t,X_d)+E_{u(n+1),LSB}(t,X_d)+E_{u(n+2),LSB}(t,X_d)+E_{u(n+3)}^{uplink}+E_{u(n+4)}^{uplink}$$

$$\propto 2\sqrt{(1-a_{opd})P_{cn}}J_0(\beta\pi)\times\{b_{-1}e^{j\left(\psi_{0,n}(t,X_d)-\phi_{un}(t)-\frac{\pi}{4}\right)}$$

$$+b_0e^{j(\psi_{0,n}(t,X_d)-\frac{\pi}{4})}\}$$

$$+2\sqrt{(1-a_{opd})P_{c(n+1)}}J_0(\beta\pi)\times\{b_{-1}e^{j\left(\psi_{0,n+1}(t,X_d)-\phi_{c(n+1)}(t)-\frac{\pi}{4}\right)}$$

$$+b_0e^{j(\psi_{0,n+1}(t,X_d)-\frac{\pi}{4})}\}$$

$$+2\sqrt{(1-a_{opd})P_{c(n+2)}}J_0(\beta\pi)\times\{b_{-1}e^{j\left(\psi_{0,n+2}(t,X_d)-\phi_{c(n+2)}(t)-\frac{\pi}{4}\right)}$$

$$+b_0 e^{j(\psi_{0,n+2}(t,X_d)-\frac{\pi}{4})}\}$$

$$+2\sqrt{(1-a_{opd})P_{c(n+3)}}J_0(\beta\pi)e^{j\left(\psi_{0,n+3}(t,X_d)-\frac{\pi}{4}\right)}$$

$$+2\sqrt{(1-a_{opd})P_{c(n+4)}}J_0(\beta\pi)e^{j\left(\psi_{0,n+4}(t,X_d)-\frac{\pi}{4}\right)} \quad (32)$$

As noted from the uplink spectrum shown in Figure 2.8(a), because the uplink frequency $f_{un}$ is 57 GHz as an example in the demonstrated system, the optical carrier $C_{n+2}$ and the LSB subcarriers $L_n$, $C_{n+3}$ & $L_{n+1}$, and $C_{n+4}$ & $L_{n+2}$ are overlapped. As a result, the new channels within 25 GHz spacing are formed for DWDM demultiplexing at the CS, which is shown in Figure 2.8(b).

After propagating via the uplink fiber with distance of $X_u$, the optical uplink signal $E^{uplink}_{combined,LSB}(t, X_d, X_u)$ is then rewritten as

$$\begin{aligned}
E^{uplink}_{combined,LSB}(t,X_d,X_u) &= E_{un,LSB}(t,X_d)\cdot\exp\{-j\beta_{u,n}(f)\cdot X_u\} \\
&+ E_{u(n+1),LSB}(t,X_d)\cdot\exp\{-j\beta_{u,n+1}(f)\cdot X_u\} \\
&+ E_{u(n+2),LSB}(t,X_d)\cdot\exp\{-j\beta_{u,n+2}(f)\cdot X_u\} \\
&+ E^{uplink}_{c(n+3)}(t,X_d)\cdot\exp\{-j\beta_{u,n+3}(f)\cdot X_u\} \\
&+ E^{uplink}_{c(n+4)}(t,X_d)\cdot\exp\{-j\beta_{u,n+4}(f)\cdot X_u\} \\
&\propto 2\sqrt{(1-a_{opd})P_{cn}}J_0(\beta\pi)\times\{b_{-1}e^{jv_{0,-1,n}(t,X_d,X_u)} \\
&+ b_0 e^{jv_{0,0,n}(t,X_d,X_u)}\}
\end{aligned}$$

$$
\begin{aligned}
&+2\sqrt{(1-a_{opd})P_{c(n+1)}}J_0(\beta\pi)\times\{b_{-1}e^{jv_{0,-1,n+1}(t,X_d,X_u)}\\
&+b_0e^{jv_{0,0,n+1}(t,X_d,X_u)}\}\\
&+2\sqrt{(1-a_{opd})P_{c(n+2)}}J_0(\beta\pi)\times\{b_{-1}e^{jv_{0,-1,n+2}(t,X_d,X_u)}\\
&+b_0e^{jv_{0,0,n+2}(t,X_d,X_u)}\}\\
&+2\sqrt{(1-a_{opd})P_{c(n+3)}}J_0(\beta\pi)e^{jv_{0,0,n+3}(t,X_d,X_u)}\\
&+2\sqrt{(1-a_{opd})P_{c(n+4)}}J_0(\beta\pi)e^{jv_{0,0,n+4}(t,X_d,X_u)}
\end{aligned}
\tag{33}
$$

where $v_{0,r,n}(t,X_d,X_u)$ is defined as [5]

$$
\begin{aligned}
v_{0,r,n}(t,X_d,X_u)&=\varphi_{cn}(t)+r\phi_{un}-\beta_{d,n}(f)\cdot X_d-\beta_{u,n}(f)\cdot X_u\\
&\approx 2\pi(f_{cn}+rf_{un})(t-\beta_{d1,n}X_d-\beta_{u1,n}X_u)\\
&+\phi_{cn}(t-\beta_{d1,n}X_d-\beta_{u1,n}X_u)+r\theta_{un}(t-\beta_{d1,n}X_d-\beta_{u1,n}X_u)\\
&-\frac{1}{2}\beta_{u2,n}\cdot\{2\pi(rf_{un})\}^2\cdot X_u-[\beta_{d0.n}-\beta_{d1,n}\cdot 2\pi(f_{cn}+rf_{un})]\cdot X_d\\
&-\{\beta_{u0.n}-\beta_{u1,n}\cdot 2\pi f_{cn}\}\cdot X_u
\end{aligned}
\tag{34}
$$

As previously, the propagation constant of $\beta_{u,n}(f)$ is approximated as [14]

$$
\beta_{u,n}(f)\approx\beta_{u0,n}+\beta_{u1,n}\cdot 2\pi(f-f_{cn})+\frac{1}{2}\beta_{u2,n}\cdot\{2\pi(f-f_{cn})\}^2 \tag{35}
$$

Here, $\beta_{u1,n}X_u$ corresponds to the group-delay time and $\beta_{u2,n}$ is related with the uplink fiber dispersion parameter $D_{u,n}$ as

$$
\beta_{u2.n}=\frac{\lambda_{cn}^2}{2\pi c}\cdot D_{u,n} \tag{36}
$$

The DWDM demultiplexer with channel spacing of 25 GHz in the CS separates the three channels as described previously, $C_{n+2}$ & $L_n$, $C_{n+3}$ & $L_{n+1}$, and $C_{n+4}$ & $L_{n+2}$.

After beating at the photodiode of each channel, three photocurrents are generated and expressed as

$$i^{uplink}_{c(n+2),Ln}(t,X_d,X_u)=4R_c(1-a_{opd})\sqrt{P_{cn}P_{c(n+2)}}J_0^2(\beta\pi)e^{i\psi_{c(n+2),Ln}(t,X_d,X_u)} \tag{37}$$

$$i^{uplink}_{c(n+3),Ln+1}(t,X_d,X_u)=4R_c(1-a_{opd})\sqrt{P_{c(n+1)}P_{c(n+3)}}J_0^2(\beta\pi)e^{i\psi_{c(n+3),Ln+1}(t,X_d,X_u)} \tag{38}$$

$$i^{uplink}_{c(n+4),Ln+2}(t,X_d,X_u)=4R_c(1-a_{opd})\sqrt{P_{c(n+2)}P_{c(n+4)}}J_0^2(\beta\pi)e^{i\psi_{c(n+4),Ln+2}(t,X_d,X_u)} \tag{39}$$

where $R_c$ is the responsivity of the photodiode in the CS; $\psi_{c(n+2),Ln}(t,X_d,X_u)$, $\psi_{c(n+3),Ln+1}(t,X_d,X_u)$ and $\psi_{c(n+4),Ln+2}(t,X_d,X_u)$ are respectively defined as

$$\begin{aligned}\psi_{c(n+2),Ln}(t,X_d,X_u)&=\nu_{0,0,n+2}(t,X_d,X_u)-\nu_{0,-1,n}(t,X_d,X_u)\\&\approx 2\pi(f_{c(n+2)}-f_{cn}+f_{un})(t-\beta_{d1,n+2}X_d-\beta_{u1,n+2}X_n)\\&\quad+\phi_{c(n+2)}(t-\beta_{d1,n+2}X_d-\beta_{u1,n+2}X_u)-\phi_{cn}(t-\beta_{d1,n}X_d-\beta_{u1,n}X_u)\\&\quad+\theta_{un}(t-\beta_{d1,n}X_d-\beta_{u1,n}X_u)\\&\quad+\frac{1}{2}\beta_{u2,n}\cdot\{2\pi(f_{un})\}^2\cdot X_u+\beta_{d1,n}\cdot 2\pi f_{un}\cdot X_d\end{aligned} \tag{40}$$

$$\begin{aligned}\psi_{c(n+3),Ln+1}(t,X_d,X_u)&=\nu_{0,0,n+3}(t,X_d,X_u)-\nu_{0,-1,n+1}(t,X_d,X_u)\\&\approx 2\pi(f_{c(n+3)}-f_{c(n+1)}+f_{u(n+1)})(t-\beta_{d1,n+3}X_d-\beta_{u1,n+1}X_u)\\&\quad+\phi_{c(n+3)}(t-\beta_{d1,n+3}X_d-\beta_{u1,n+3}X_u)-\phi_{c(n+1)}(t-\beta_{d1,n+1}X_d-\beta_{u1,n+1}X_u)\\&\quad+\theta_{u(n+1)}(t-\beta_{d1,n+1}X_d-\beta_{u1,n+1}X_u)\\&\quad+\frac{1}{2}\beta_{u2,n+1}\cdot\{2\pi(f_{u(n+1)})\}^2\cdot X_u+\beta_{d1,n+3}\cdot 2\pi f_{u(n+1)}\cdot X_d\end{aligned} \tag{41}$$

$$\begin{aligned}\psi_{c(n+4),Ln+2}(t,X_d,X_u)&=\nu_{0,0,n+4}(t,X_d,X_u)-\nu_{0,-1,n+2}(t,X_d,X_u)\\&\approx 2\pi(f_{c(n+4)}-f_{c(n+2)}+f_{u(n+2)})(t-\beta_{d1,n+4}X_d-\beta_{u1,n+2}X_u)\end{aligned}$$

$$+\phi_{c(n+4)}(t-\beta_{d1,n+4}X_d-\beta_{u1,n+4}X_u)-\phi_{c(n+2)}(t-\beta_{d1,n+2}X_d-\beta_{u1,n+2}X_u)$$

$$+\theta_{u(n+2)}(t-\beta_{d1,n+2}X_d-\beta_{u1,n+2}X_u)$$

$$+\frac{1}{2}\beta_{u2,n+2}\cdot\{2\pi(f_{u(n+2)})\}^2\cdot X_u+\beta_{d1,n+4}\cdot 2\pi f_{u(n+2)}\cdot X_d \qquad (42)$$

Assuming the variation of propagation constants $\beta_{u2,n}, \beta_{u2,n+1}, \beta_{u2,n+2}, \beta_{u2,n+3}$ and $\beta_{d2,n+4}$ with the wavelength $\lambda_{cn}$ , $\lambda_{c(n+1)}$ , $\lambda_{c(n+2)}$ , $\lambda_{c(n+3)}$ and $\lambda_{c(n+4)}$ is neglected and $f_{u(n+2)}=f_{u(n+1)}=f_{un}=57GHz$ ; $f_{c(n+2)}-f_{cn}$ , $f_{c(n+2)}-f_{cn}$ and $f_{c(n+2)}-f_{cn}$ are equal to (-50GHz) because the channel spacing of DWDM is 25 GHz, the frequency components, $f_{c(n+2)}-f_{cn}+f_{un}$ , $f_{c(n+3)}-f_{c(n+1)}+f_{u(n+1)}$ and $f_{c(n+4)}-f_{c(n+2)}+f_{u(n+2)}$ , are equal to 7 GHz as shown in Figure 2.8(b), which are selected by a bandpass filter and input to the following demodulator. If the payload data, $\theta_{u(n+2)}(t)$ , $\theta_{u(n+1)}(t)$ and $\theta_{un}(t)$ , are differentially encoded, i.e. DPSK modulated in the demonstrated system, the RF uplink signal can be decoded by differential detection scheme without any serous dispersion degradation.

However, as noted in eqs.(40), (41) and (42), the laser phase noise terms, $\phi_{c(n+2)}(t)-\phi_{cn}(t)$ , $\phi_{c(n+3)}(t)-\phi_{c(n+1)}(t)$ and $\phi_{c(n+4)}(t)-\phi_{c(n+2)}(t)$ , cannot be cancelled because the laser noises originate from the different light sources. As a result, this is a limiting factor on the system performance. In order to investigate the extent of laser phase noise effect, the simulation is performed in two different cases: the ideal case [$\phi_{cn}(t)-\phi_{c(n+2)}(t)=0$] and the actual case [$\phi_{cn}(t)-\phi_{c(n+2)}(t)\neq 0$].

In general, the DWDM configuration of downlink and uplink is introduced. In the downlink direction, the system principle of downlink spectrum is described how the MZ modulator generates the DSB spectrum before multiplexing by the DWDM multiplexer. After applying the optical bandpass filter, three adjacent optical channels and corresponding subcarriers are selected to have the 60 GHz signal generated. As a measure to simplify the architecture of BS by removing the laser in the BS, the remote light source is obtained from the downlink spectrum and used as local light for uplink transmission. In addition, the mathematical expression is used to describe the spectrum generation, propagation, and signal processing. On the other hand, in the uplink direction, the EA modulator uses the remote light to modulate the RF subcarrier on the optical carrier to generate the SSB spectrum. After combining all the uplink SSB spectrum, the new channels are formed for the DWDM demultiplexing implemented at the CS. However, the 60 GHz band signal is transmitted in the uplink, the 7 GHz signal is processed at the CS because the new DWDM channel is formed.

# Chapter 3 Simulation Set Up

## 3.1 Downlink Set Up

### 3.1.1 Downlink Spectrum

In the demonstrated system, the simulation system is configured to function as the full- duplex DWDM system with 1 central station and 3 base stations. In the downlink system as shown in Fig.2.2, 5 optical carriers with channel spacing of 25 GHz for DWDM multiplexing are transmitted at wavelengths of ?$_1$=1553.5 nm, ?$_2$=1553.7nm, ?$_3$=1553.9nm, ?$_4$=1554.1 nm, and ?$_5$=1554.3 nm, respectively. The ideal linewidth (=0) of CW laser is configured in the simulation.

Two pseudorandom bit sequences (PRBS) of $2^{23}$-1 are set up as data source. Two DPSK modulators modulate two data sources at frequency $f_d = 10GHz$ to generate the

LSB and USB subcarrier. In order to generate optical single sideband (OSSB), a 4-port $90^0$ hybrid [13], detailed in Figure 3.1, is used before a MZ modulator.

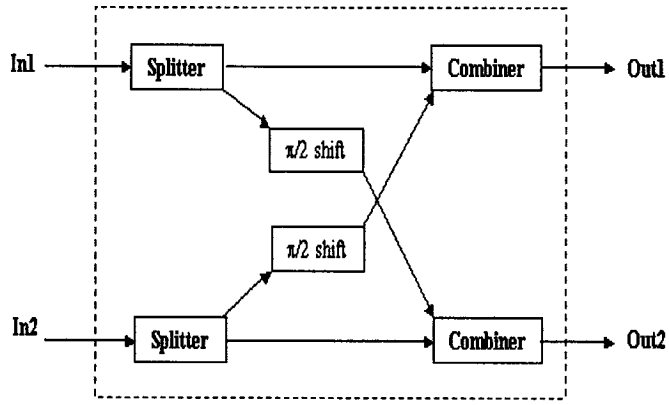


Figure 3.1 4 port $90^0$ hybrid

The LSB signal applied to In1 and the USB signal applied to In2, which are shown in Figure 3.1, are split into two components by the $90^0$ hybrid, respectively. One part of LSB signal is shifted by $\pi/2$ on one arm of $90^0$ hybrid and then combined with another part of USB signal without $\pi/2$ shifts, vice versa. The MZ modulator biased at the quadrature point [13] transfers the one output of $90^0$ hybrid as the USB subcarrier and another output as the LSB subcarrier. As a result, the DSB signal is generated and located on the both side of the optical carrier as shown in Figure 3.2, where $C_3$ represents the optical carrier at wavelength $\lambda_3 = 1553.9nm$ and $U_3 \& L_3$ represent the USB subcarrier at wavelength 1553.82nm and LSB at wavelength 1553.98nm, respectively.

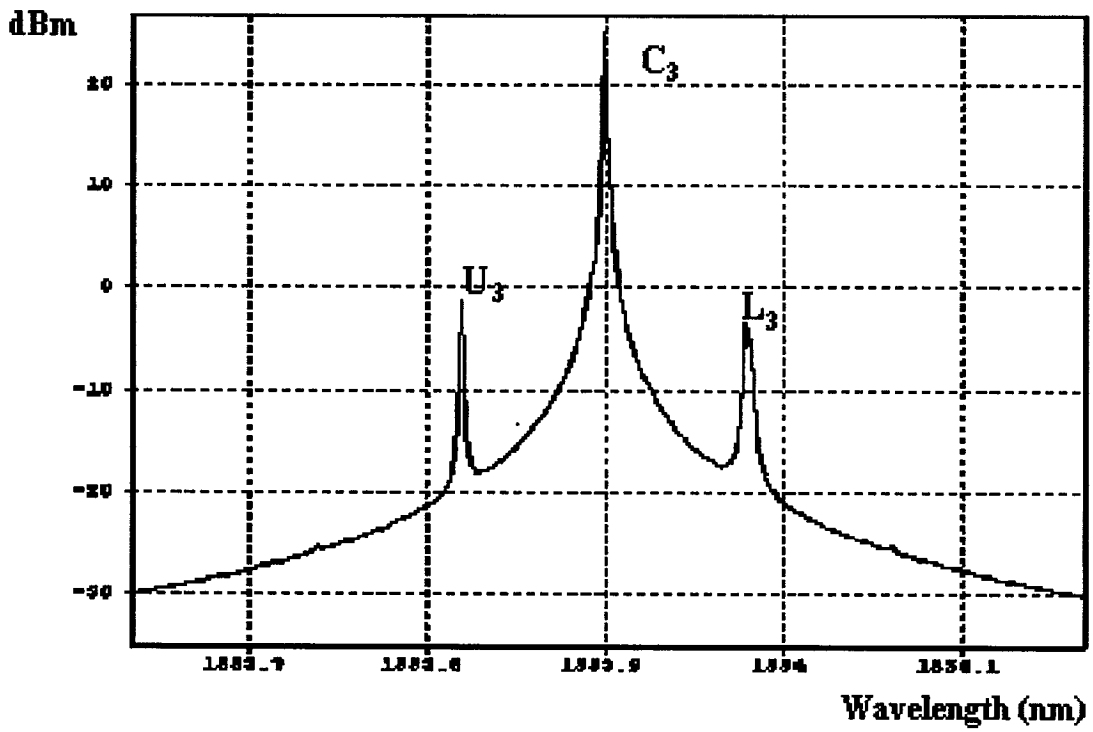


Figure 3.2 Output spectrum after MZ modulator at $\lambda_3 = 1553.9nm$

The awareness of inter-modulation distortion has to be paid attention. This is mainly due to the non-linearity characteristics of opto-electronics modulator. As for a dual arm MZ modulator using for an OSSB generation, if the modulator is modulated by a single-frequency signal $\cos 2\pi f_d t$, the output field is expressed as follows [8]

$$E_0 = \frac{E_i}{2}\left\{\cos\left[2\pi f_c t + \frac{\pi}{2} + \beta\pi \cos(2\pi f_d t)\right] + \cos\left[2\pi f_c t + \beta\pi \cos\left(2\pi f_d t + \frac{\pi}{2}\right)\right]\right\}$$

$$= \frac{E_i}{2}\{\sqrt{2}J_0(\beta\pi)\sin\left(2\pi f_c t - \frac{\pi}{4}\right)$$

$$-2J_1(\beta\pi)\cos[2\pi(f_c + f_d)t]$$

$$+2J_2(\beta\pi)\sin[2\pi(f_c - 2f_d)t]$$

$$+2J_3(\beta\pi)\sin[2\pi(f_c-3f_d)t]$$

$$+.....\}$$

where $E_i(t)$ is the input optical field, $f_c$ is the optical carrier frequency, $f_d$ is the RF frequency of the subcarrier, and $\beta\pi = \pi V_{ac}/V_\pi$ is the normalized amplitude of the RF drive signal. $V_\pi$ is the switching voltage of MZ modulator and $V_{ac}$ is the amplitude of DPSK signal. Because the MZ modulator does not have a linear transfer function, the high order harmonics can be generated if the modulation depth $\beta\pi$ is too high; this introduces crosstalk between channels after the DWDM multiplexer. In practice, $\beta\pi << 1$ is maintained so that the $J_1(\beta\pi)$ term is much high than second or high order harmonics. For example, $V_{ac}$ is 0.6 V and $\beta\pi = 0.27$ is maintained in the demonstrated system.

However, in order to generate the DSB signal, two RF signals output from $90^0$ hybrid are simultaneously applied to the MZ modulator which is biased at the quadrature point $V_\pi/2$. Table 3.1 shows the bias voltage used in the demonstrated system.

Table 3.1 Bias voltage of MZ modulator

| Wavelength of optical carrier (nm) | Bias voltage of MZ modulator (V) with $V_\pi = 7V$ |
|---|---|
| 1553.7 | 3.5 |
| 1553.9 | 3.5 |
| 1554.1 | 3.5 |
| 1554.3 | 3.5 |

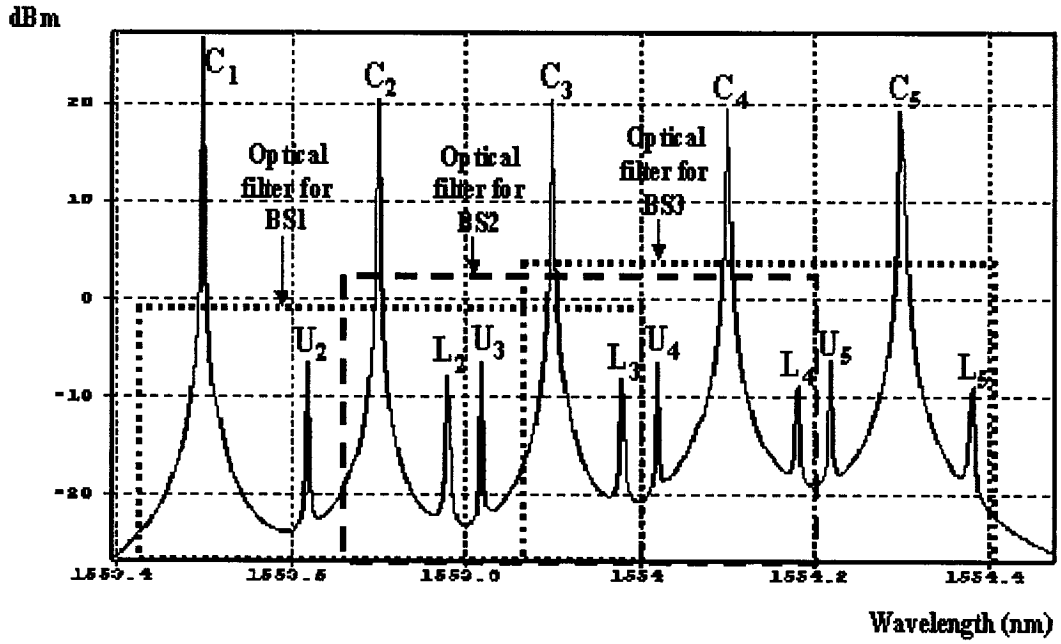


Figure 3.3 Downlink spectrum output from the DWDM multiplexer

A DWDM multiplexer combines all the optical carriers and corresponding subcarriers and transmits to the downlink fiber. The downlink spectrum after the DWDM multiplexer is shown in Figure 3.3, which consists of 5 optical carriers ($C_1$, $C_2$, $C_3$, $C_4$, and $C_5$) and subcarriers ($U_2$, $L_2$, $U_3$, $L_3$, $U_4$, $L_4$, $U_5$ and $L_5$), where $C_1$, $C_2$, $C_3$, $C_4$ and $C_5$ represent optical carriers at wavelength of $\lambda_1$, $\lambda_2$, $\lambda_3$, $\lambda_4$, and $\lambda_5$; $U_2$, $L_2$, $U_3$, $L_3$, $U_4$, $L_4$, $U_5$ and $L_5$ represent the upper sideband ($f_{cn} + f_d$) subcarriers and lower sideband ($f_{cn} - f_d$) subcarriers of corresponding optical carrier respectively, $n = 2,3,4,5$ and $f_d = 10GHz$ is radio frequency of each subcarrier. Note that no subcarriers are modulated on the optical carrier $C_1$ that is only used as a reference wavelength of photodiode in the base station 1.

### 3.1.2 Optical Bandpass Filter

The optical bandpass filter is designed as channel selection scheme for each base station. Three adjacent channels and corresponding LSB and USB subcarriers determine the bandwidth of optical band-pass filter. However, as described in Eq.(24), the USB subcarrier of the first channel has to be excluded because it causes the crosstalk on the 60 GHz signal. In addition, the wavelength of the first channel is the reference wavelength of a photodiode as well.

The lower frequency of the filter locates at the edge of the LSB subcarrier of third channel and the upper frequency locates at the edge of optical carrier of first channel. As shown in Figure 3.3, the optical filter for BS1 is located between the optical carrier $C_1$ and the subcarrier $L_3$; the optical filter for BS2 is located between the optical carrier $C_2$ and the subcarrier $L_4$ and the optical filter for BS3 is located between the optical carrier $C_3$ and the subcarrier $L_5$. After the downlink spectrum passes each optical bandpass filter, the output spectrum of each base station are shown in Figure 3.4.

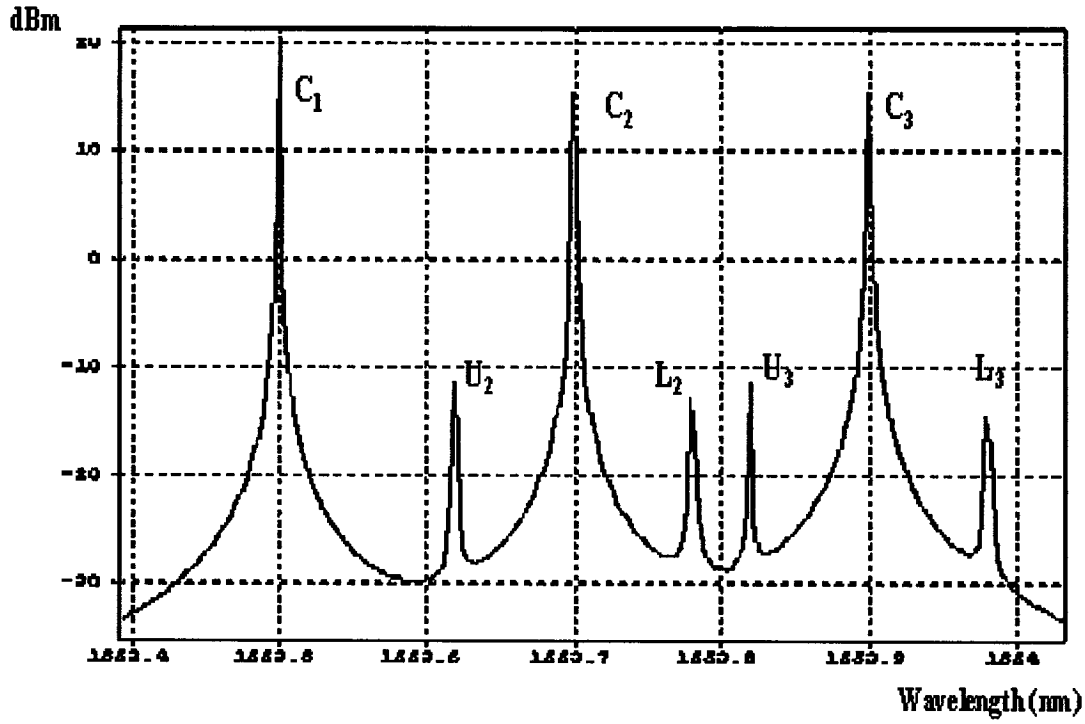
dBm
C1
C2
C3
U2
L2
U3
L3
Wavelength (nm)

(a)

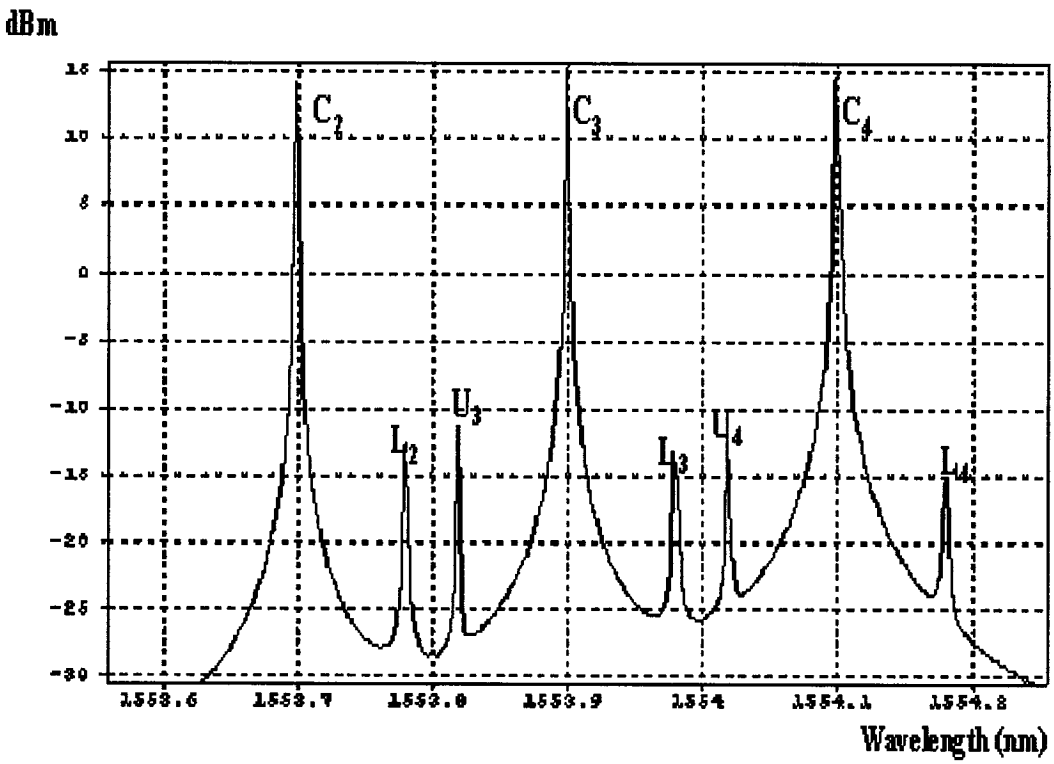
dBm
C1
C3
C4
U3
L2
L3
U4
L4
Wavelength (nm)

(b)

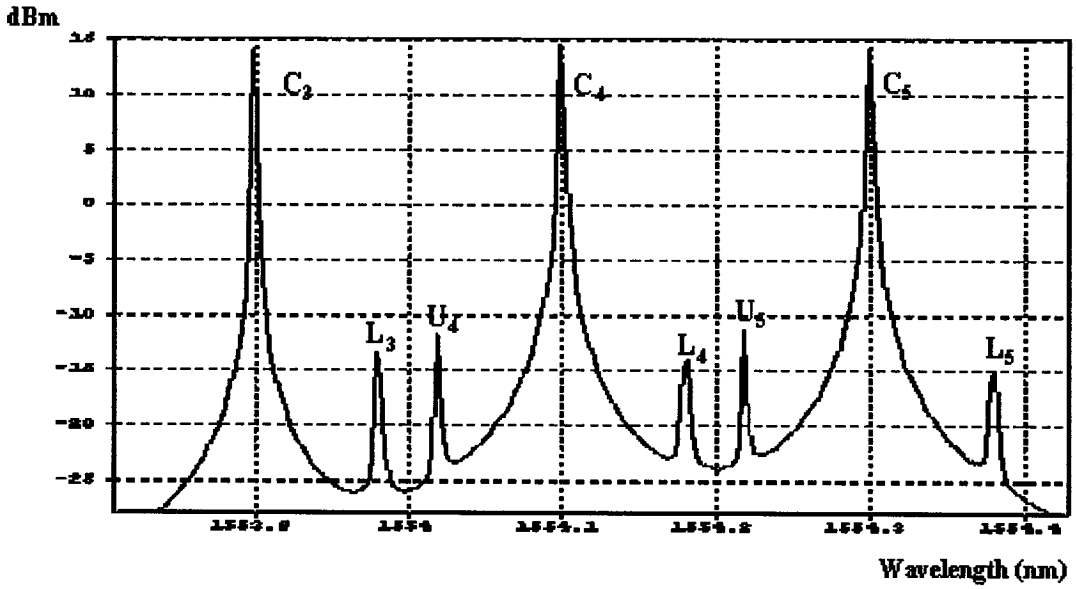


(c)

Figure 3.4 Spectrum after optical filter (a) Base station 1; (b) Base station 2; (c) Base station 3.

The spectra shown in Figure 3.4 are for base station 1, 2 and 3 respectively. Table 3.2 lists the wavelength of optical carriers and subcarriers.

Table 3.2 The wavelength of optical carriers and subcarriers

| Optical carrier wavelength (nm) | Upper sideband subcarrier ( $f_{cn} + f_d$ ) wavelength (nm) | Lower sideband subcarrier ( $f_{cn} - f_d$ ) wavelength (nm) |
|---|---|---|
| $\lambda_1 = 1553.5nm$ | | |
| $\lambda_2 = 1553.7nm$ | 1553.62 | 1553.78 |
| $\lambda_3 = 1553.9nm$ | 1553.82 | 1553.98 |
| $\lambda_4 = 1554.1nm$ | 1554.02 | 1554.18 |
| $\lambda_5 = 1554.3nm$ | 1554.22 | 1554.38 |

The Raised-Cosine bandpass filter with bandwidth of 63 GHz is configured as the optical bandpass filters in each BS because it features the lower insertion loss on the band edge of bandwidth, where the optical carrier $C_1$ and the subcarrier $L_3$, $C_2$ & $L_4$, and $C_3$ & $L_5$ are located. Table 3.3 illustrates the parameters for each optical bandpass filter.

Table 3.3 The parameters of optical bandpass filter

| Filter type | | Optical carriers and subcarriers to be included within the bandwidth | Center Frequency (nm) | Bandwidth (nm) |
|---|---|---|---|---|
| Raised-Cosine bandpass filter | | | | |
| Raised-Cosine Exponent | Raised-Cosine Roll off | | | |
| 1 | 0.1 | $C_1, C_2, C_3, U_2, L_2, U_3, L_3$ | 1553.74 | 0.51 |
| 1 | 0.1 | $C_2, C_3, C_4, L_2, U_3, L_3, U_4, L_4$ | 1553.94 | 0.51 |
| 1 | 0.1 | $C_3, C_4, C_5, L_3, U_4, L_4, U_5, L_5$ | 1554.14 | 0.51 |

### 3.1.3 Downlink Photodetection

After filtered out by each optical bandpass filter, the optical carriers and corresponding subcarriers are split by the 90/10-power divider. The 10% of power is applied to each photodiode in the base station for photodetection. The 90% of power is reserved as the light source for uplink transmission. The photodiode of each base station features PIN typed and wideband. Figure 3.5 illustrates the electrical spectra after photodetection in each base station.

Seven electrical spectra as shown in Figure 3.5 at different frequencies are generated after photodetection in the each base station but only the 60 GHz signal is interested. Figure 3.5 (a) shows the 60 GHz signal generated after beating between the optical carriers $C_1$ and the LSB subcarrier $L_3$; Figure 3.5 (b) shows the 60 GHz signal generated after beating between the optical carrier $C_2$ and the subcarrier $L_4$, and Figure 3.5 (c) shows the 60 GHz signal generated after beating between the optical carrier $C_3$ and the subcarrier $L_5$, respectively.

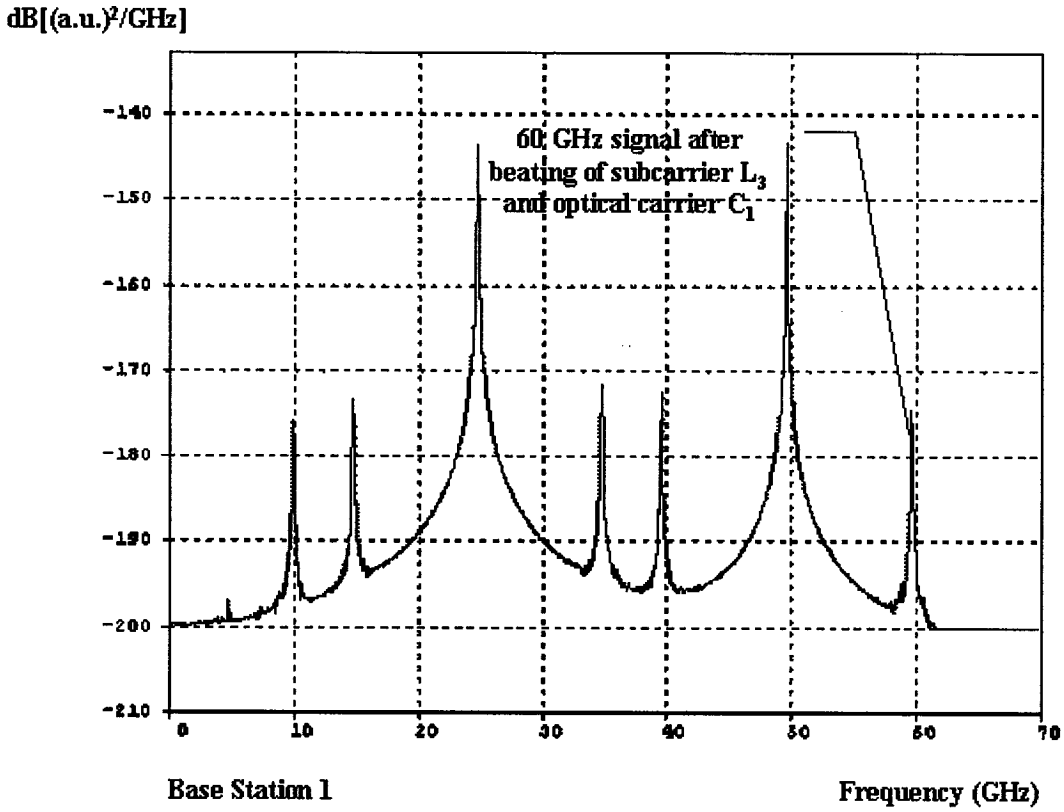


(a)

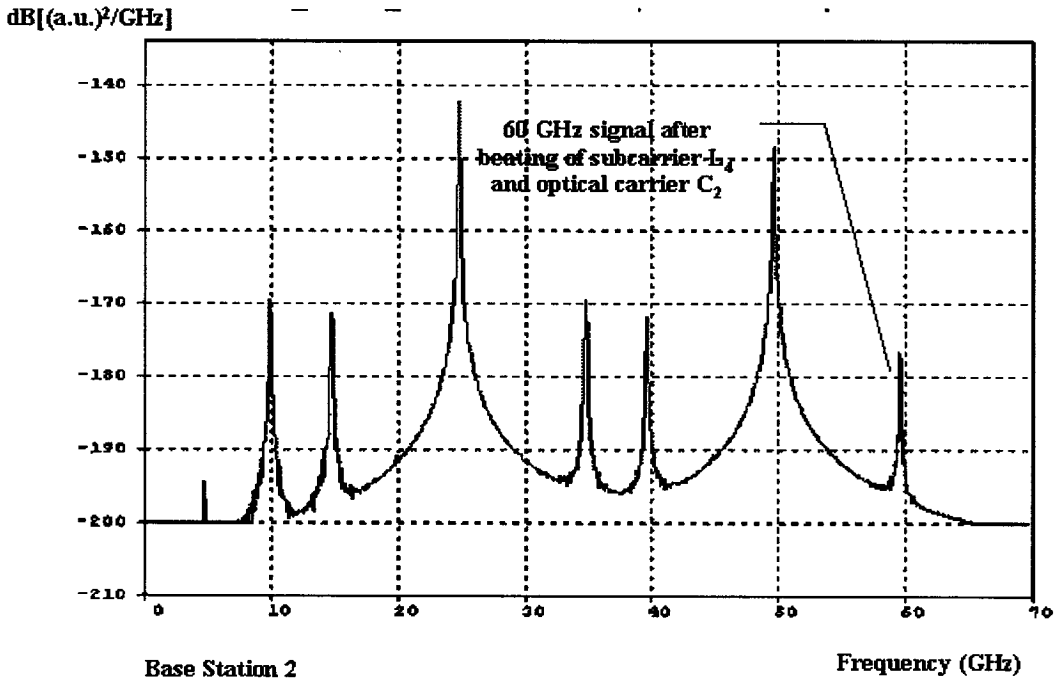


(b)

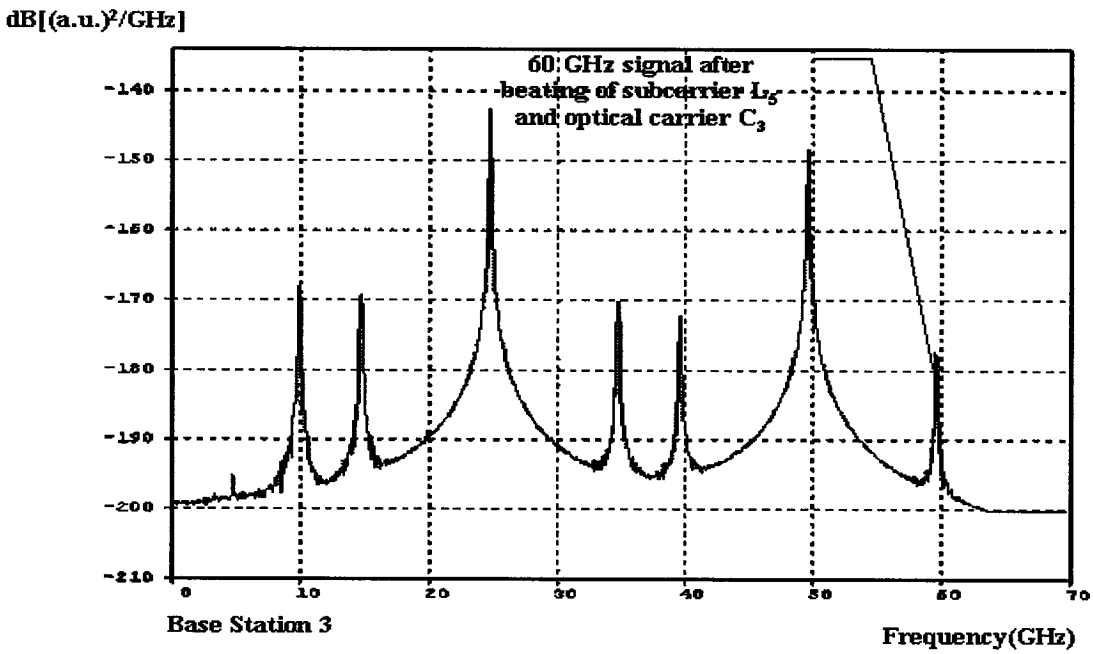


(c)

Figure 3.5 Electrical spectra after photodetection (a) Spectrum in the base station 1; (b) Spectrum in the base station 2; (c) Spectrum in the base station 3.

### 3.1.4 Electrical Bandpass Filter

In the demonstrated system, an electrical bandpass filter selects 60 GHz signal before sending to DPSK demodulator for further processing. Importantly, the bandwidth of electrical bandpass filter is not determined by the 3-dB bandwidth of 60GHz signal spectrum. The bandwidth optimization is described in section 4.1.

The Butterworth bandpass filter is configured as the electrical bandpass filters because it dose not cause the distortion on the eye diagram that is to evaluate the receiver performance and the better Q value is achieved. In addition, the number of poles is optimized for this reason as well.

Table 3.4 lists the property of Butterworth bandpass filters used in each base station.

Table 3.4 The property of Butterworth bandpass filters used in each base station.

| Base station | Centre frequency (GHz) | Number of poles | 3 dB bandwidth (GHz) |
|---|---|---|---|
| 1 | 59.6 | 4 | 1.5 |
| 2 | 59.6 | 4 | 2 |
| 3 | 59.6 | 6 | 1.5 |

### 3.1.5 DPSK Demodulator

Asynchronous demodulation scheme [17] is used for the demodulation. The delay scheme of DPSK format is suitable for DPSK demodulator to use the asynchronous demodulation scheme. The 60GHz signal is multiplied by the replica of it that has been delayed by one bit period. However, the phase stability over a few bits is required and can be satisfied by implementing the DFB laser.

In addition, lowpass filter is to remove the high frequency components of recovered signal after the DPSK demodulator as shown in Figure 3.6 demodulates the 60GHz signal.

The reason why the Bessel low pass filter is chosen as the lowpass filter is that the distortion of eye diagram caused by it is less and the better Q value is achieved. In addition, the number of poles is optimized for this reason as well.

Table 3.5 lists the property of Bessel lowpass filter for each receiver.

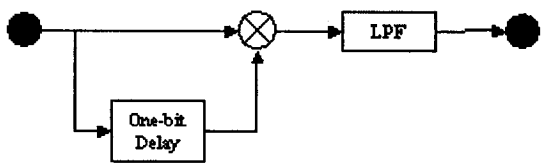


Figure 3.6 DPSK demodulator

Table 3.5 The property of Bessel lowpass filter for each receiver

| Base station | Number of poles | 3 dB bandwidth (GHz) |
|---|---|---|
| 1 | 5 | 0.1 |
| 2 | 5 | 0.1 |
| 3 | 5 | 0.1 |

### 3.1.6 Downlink Simulation Results

The eye diagram is to qualify the performance of receiver. Figure 3.7 (a) shows the eye diagram with the Q value of 40 dB while the received power level prior to the photodiode is –43.99dBm; Figure 3.7 (c) shows the recovered data after decoding the subcarrier $L_3$ in the base station 1. Therefore, by comparing the logical input data in Figure 3.7 (b), the recovered data is very similar to the input data but there is the ripple on the "1" level, which is reflected by the curvature of "1" level on the eye diagram. Moreover, the extent of curvature is proportionally related to the ripple of "1" level on the recovered data. If the curvature is bigger, that means the ripple is bigger, too. However, it can be reduced to the certain extent by adjusting the bandwidth of bandpass filter located after the photodiode.

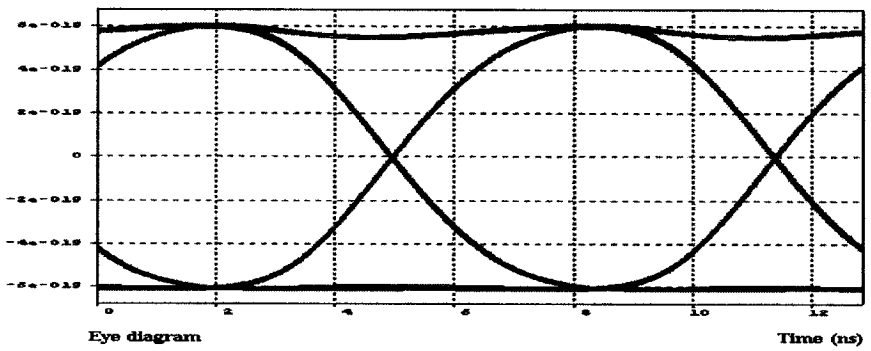


**(a)**

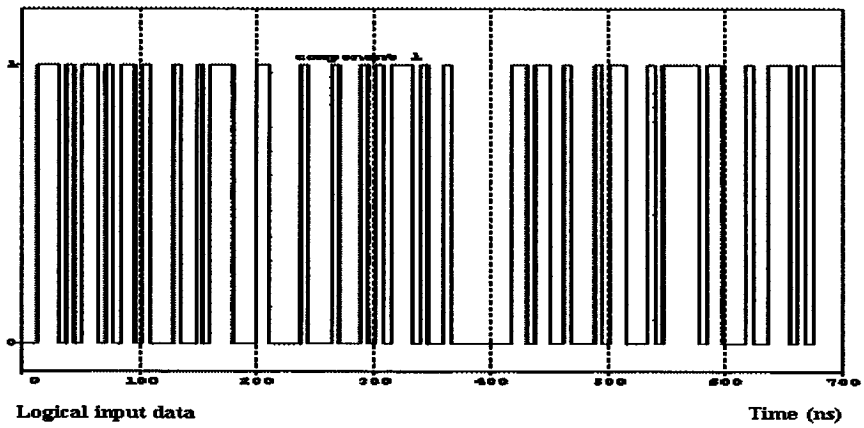


(b)

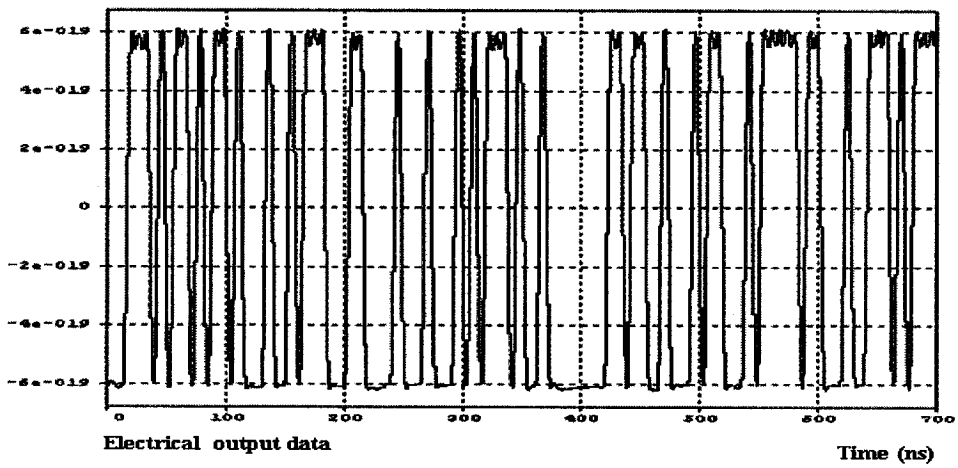


(c)

Figure 3.7 (a) Eye diagram; (b) Logical input data; (c) The output recovered data in the base station 1

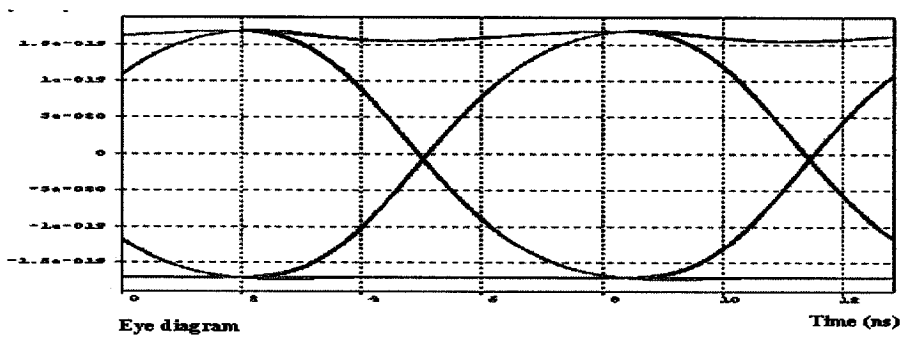


(a)

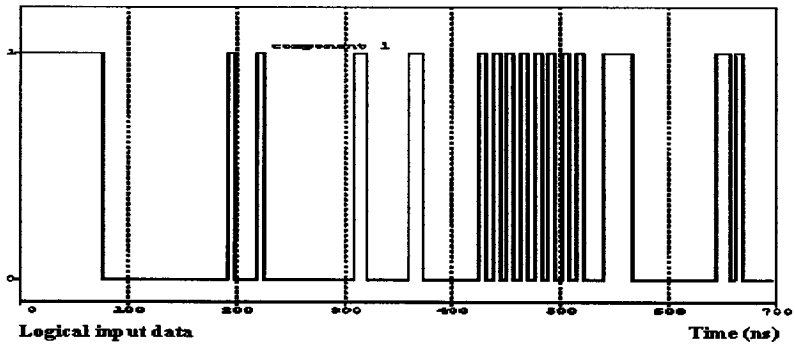


(b)

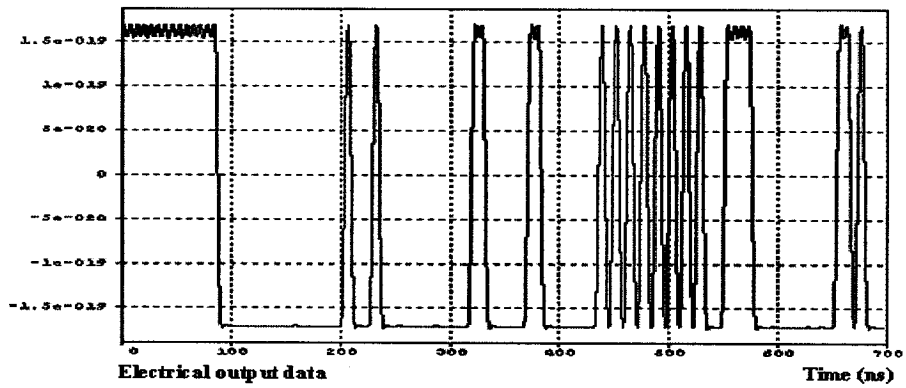


(c)

Figure 3.8 (a) Eye diagram; (b) Logical input data; (c) The recovered output data in the base station 2.

Figure 3.8 (a) shows the eye diagram in BS2 with the Q value of 40 dB while the received power level prior to the photodiode is –44.6dBm; Figure 3.8 (c) shows the recovered data after decoding the subcarrier $L_4$ in the base station 2. Therefore, by comparing the logical input data in Figure 3.8 (b), the recovered data is very similar to the input data but there is the ripple on the '1' level, which is reflected by the curvature of "1" level on the eye diagram. Moreover, the extent of curvature is proportionally related to the ripple of "1" level on the recovered data. If the curvature is bigger, that means the

ripple is bigger. However, it can be reduced to the certain extent by adjusting the bandwidth of bandpass filter after the photodiode.

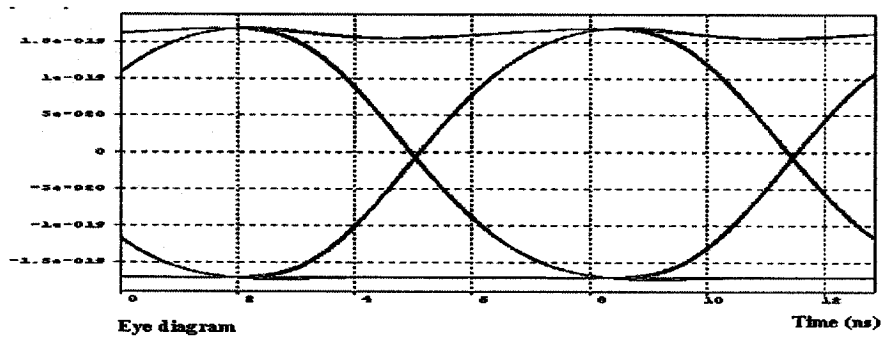


(a)

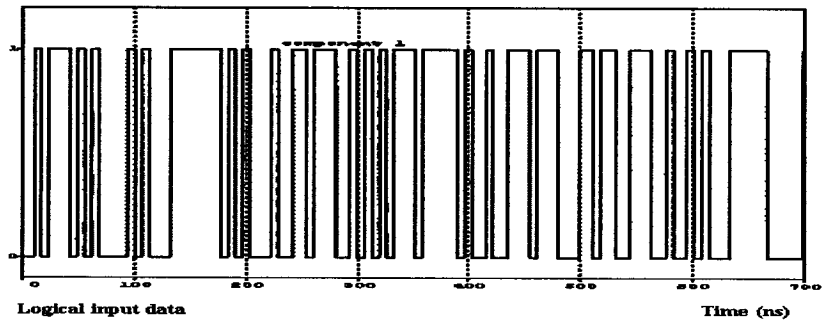


(b)

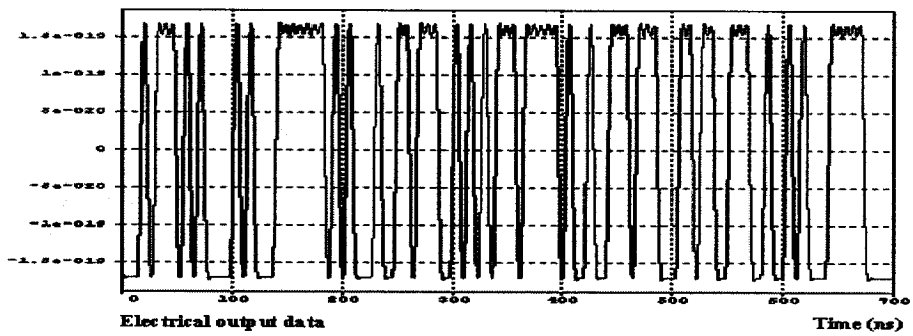


(c)

Figure 3.9 (a) Eye diagram; (b) Logical input data; (c) The recovered output data in the base station 3.

Figure 3.9 (a) shows the eye diagram with the Q value of 40dB while the received power level prior to the photodiode is –44.58dBm; Figure 3.9 (c) shows the recovered data after decoding the subcarrier $L_5$ in the base station 3. Therefore, by comparing the logical input data in Figure 3.9 (b), the recovered data is very similar to the input data but there is the ripple on the "1" level, which is reflected by the curvature of "1" level of the eye diagram. Moreover, the extent of curvature is proportionally related to the ripple of "1" level on the recovered data. If the curvature is bigger, that means the ripple is bigger. However, it can be reduced to the certain extent by adjusting the bandwidth of bandpass filter located after the photodiode.

In summary, table 3.6 lists Q value and the received power before the photodiode. As described on page 174 in [17], the BER of $10^{-9}$ can be achieved for data rate of 155.52 Mbps while the received power at photodiode is no less than –44 dBm. However, the better BER results are achieved during the simulation with same value of optical power. In general, the error free result can be achieved for the DWDM downlink system.

Table 3.6 Q value and corresponding received power before the photodiode.

| Base Station | Q value (dB) | Receiving power at photodiode (dBm) |
|---|---|---|
| 1 | 40 | -43.99 dBm |
| 2 | 40 | -44.6 dBm |
| 3 | 40 | -44.58 dBm |

## 3.2 Uplink Set Up

### 3.2.1 Optical Narrowband Bandpass Filter

In order to make the base stations simple, the remote light source from the downlink is used as the light source at each station for uplink transmission. The optical narrowband bandpass filter as shown in the uplink system configuration in figure 2.3 is implemented to select the first optical carrier of every three adjacent downlink carriers from the remained 90% of the downlink optical power, which determines the wavelength of uplink transmission for each base station. The Raised-Cosine bandpass filter with the parameters listed in Table 3.7 is chosen as the optical bandpass filter without any particular reason.

Table 3.7 The property of optical narrowband bandpass filter

| Base station | Optical bandpass filter | | | |
|---|---|---|---|---|
| | Raised-Cosine bandpass filter | | | |
| | Raised-Cosine exponent | Raised-Cosine roll-off | Center frequency (nm) | Bandwidth (nm) |
| Base Station 1 | 1 | 0.8 | 1553.5 | 0.081 |
| Base Station 2 | 1 | 0.8 | 1553.7 | 0.081 |
| Base Station 3 | 1 | 0.8 | 1553.9 | 0.081 |

As shown in Fig. 3.10, the downlink carriers, $C_1$ ( $\lambda_1 = 1553.5nm$ ), $C_2(\lambda_2 = 1553.7nm)$, and $C_3(\lambda_3 = 1553.9nm)$, are used as the uplink optical carriers for the base station 1, 2 and 3, respectively.

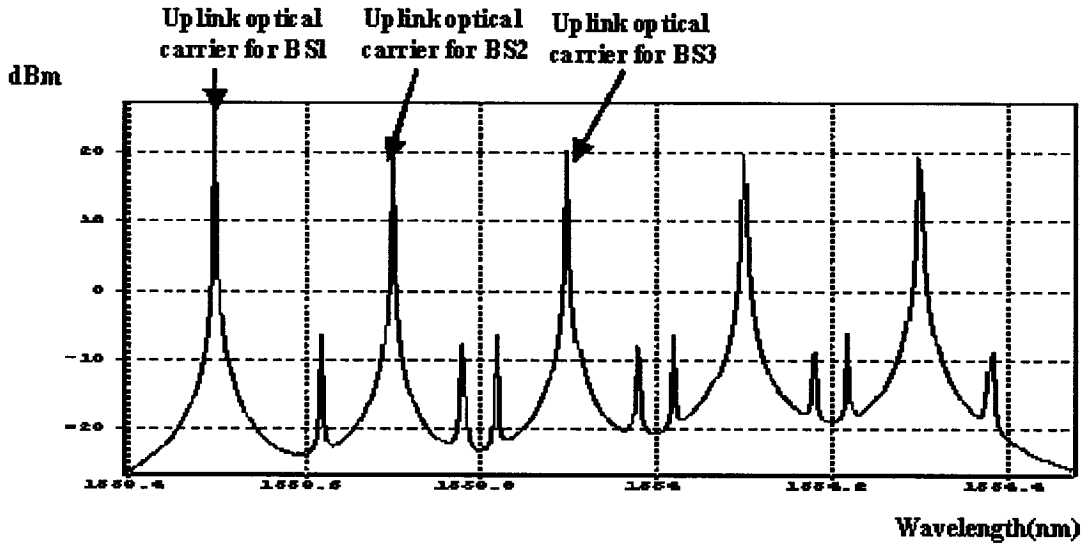


Figure 3.10 Downlink spectrum

### 3.2.2 Uplink Modulation

In the uplink direction, an external modulator, EA modulator, is used to modulate the uplink RF subcarrier at frequency $f_u = 57GHz$. In order to generate SSB spectrum, a notch filter with the parameters listed in Table 3.8 is implemented to eliminate the USB subcarrier $f_c + f_u$.

Table 3.8 The property of optical notch filter

| Base station | Optical notch filter | | | |
|---|---|---|---|---|
| | Raised-Cosine notch filter | | | |
| | Raised-Cosine exponent | Raised-Cosine roll-off | Center frequency (nm) | Bandwidth (nm) |
| Base Station 1 | 1 | 0.5 | 1553.04 | 0.16 |
| Base Station 2 | 1 | 0.5 | 1553.24 | 0.16 |
| Base Station 3 | 1 | 0.5 | 1553.44 | 0.16 |

As illustrated in Figure 3.11, the graphs display the uplink spectrum in the base station 1, 2, and 3, where $C_1$, $C_2$, and $C_3$ represent the optical carriers with same downlink wavelength respectively; $L_1^{uplink}$, $L_2^{uplink}$ and $L_3^{uplink}$ represent the uplink LSB subcarriers at frequency $f_u = 57GHz$, respectively.

As noted on the graph in Figure 3.11, after combined by the optical power combiner, the optical carrier $C_3$ is overlapped with the subcarrier $L_1^{uplink}$, $C_4$ & $L_2^{uplink}$, and $C_5$ & $L_3^{uplink}$, respectively. However, the power level of each uplink signal has to be optimized by an attenuator in order to generate the new DWDM channels within 25 GHz spacing as shown in Figure 3.11 (d). Otherwise, the LSB subcarrier $L_1^{uplink}$ cannot be observed if the power of the optical carrier $C_3$ is too high. As a result, the DWDM demultiplexer in the central station is implemented to demultiplex the uplink signal.

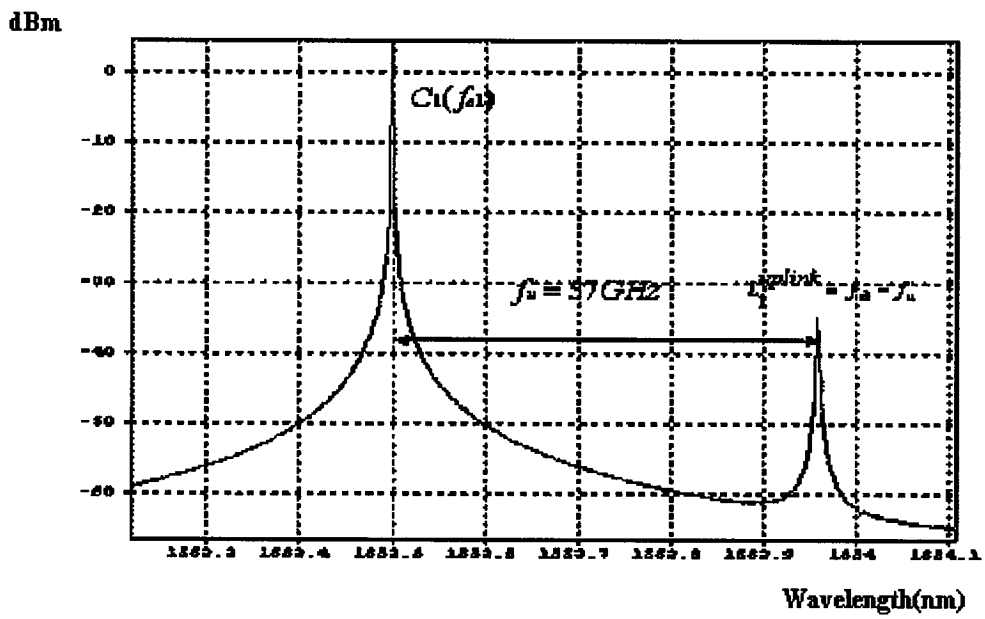


**(a)**

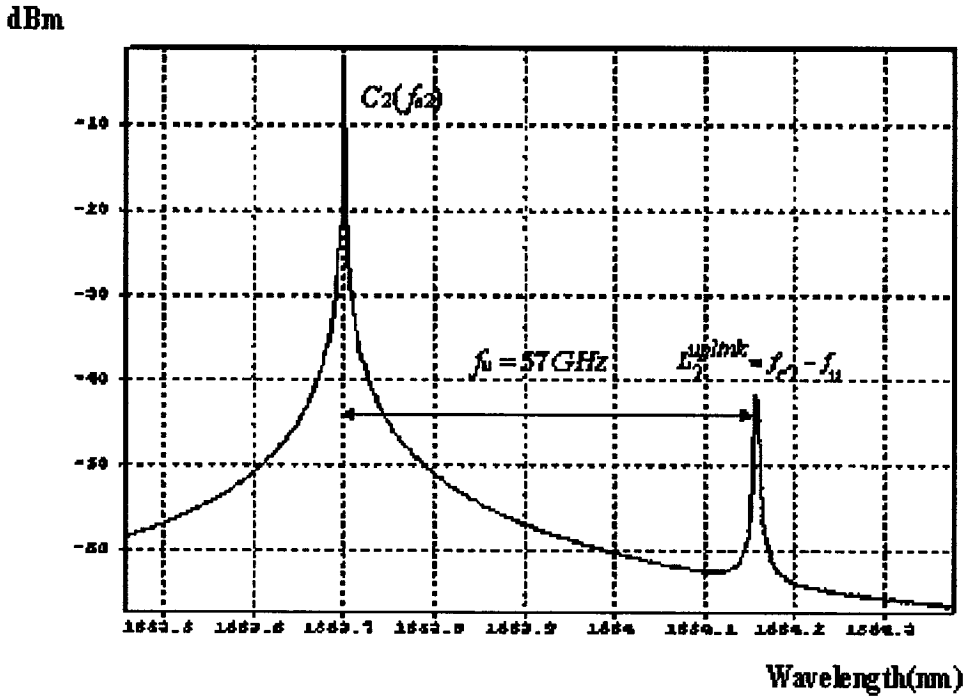
dBm
$C_2(f_{c2})$
$f_u = 57GHz$
$L_2^{uplink} = f_{c2} - f_u$
Wavelength(nm)

(b)

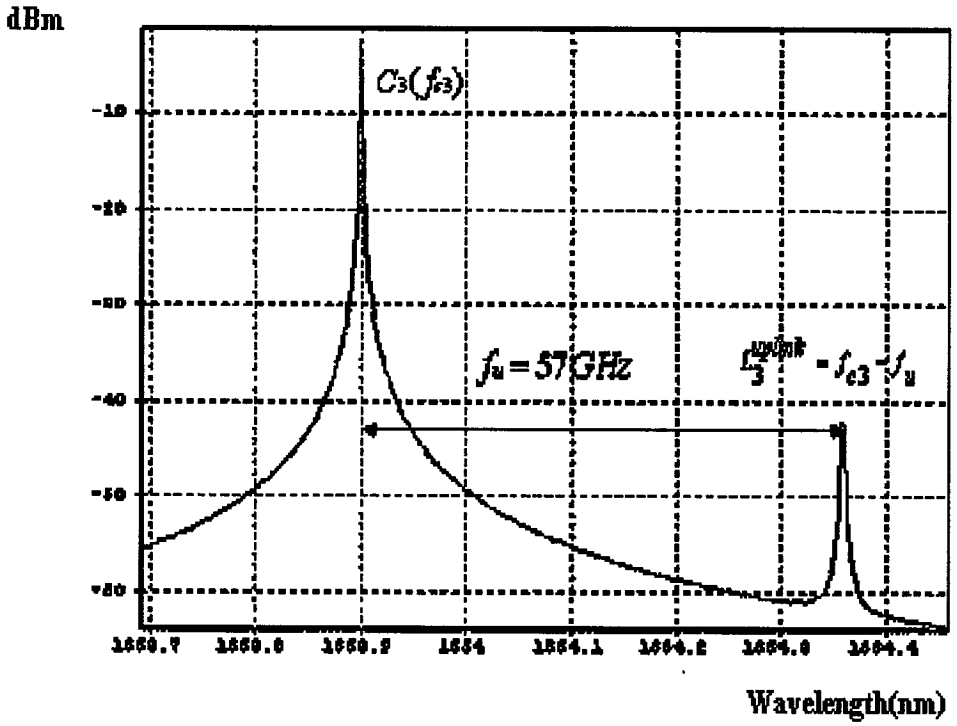
dBm
$C_3(f_{c3})$
$f_u = 57GHz$
$L_3^{uplink} = f_{c3} - f_u$
Wavelength(nm)

(c)

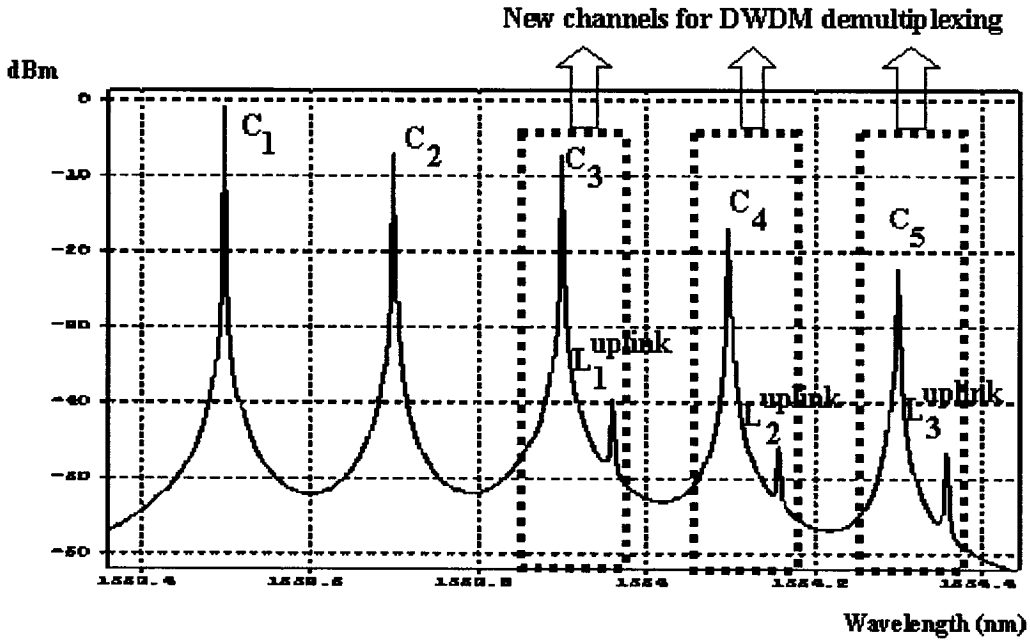


**(d)**

Figure 3.11 (a) Uplink spectrum in base station 1; (b) Uplink spectrum in base station 2; (c) Uplink spectrum in base station 3; (d) Combined uplink spectrum and the illustration of new channels formed for DWDM demultiplexing.

### 3.2.3 Uplink Photodetection

After demultiplexed by the DWDM demultiplexer in the central station, the channel of $C_3$ & $L_1$ is applied to the photodiode in BS1 and the electrical spectrum as shown in Figure 3.12 (e) is generated; the channel of $C_4$ & $L_2$ is applied to the photodiode in BS2 and the electrical spectrum as shown in Figure 3.12 (f) is generated; the channel of $C_5$ & $L_3$ is applied to the photodiode in BS3 and the electrical spectrum as shown in Figure 3.12 (g) is generated. The reference wavelength of the photodiode in each base station is configured to the wavelength of optical carrier $C_3$, $C_4$ and $C_5$,

respectively. As configured in the demonstrated system with the radio frequency of uplink subcarriers ( $f_u = 57GHz$ ), the 7GHz electrical signal is generated after beating operation in the photodiode.

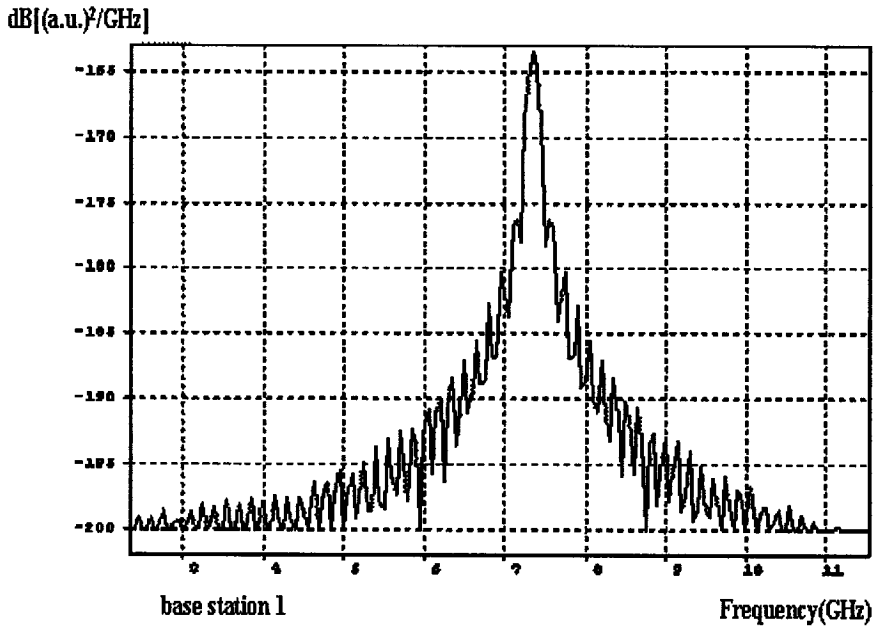


(e)

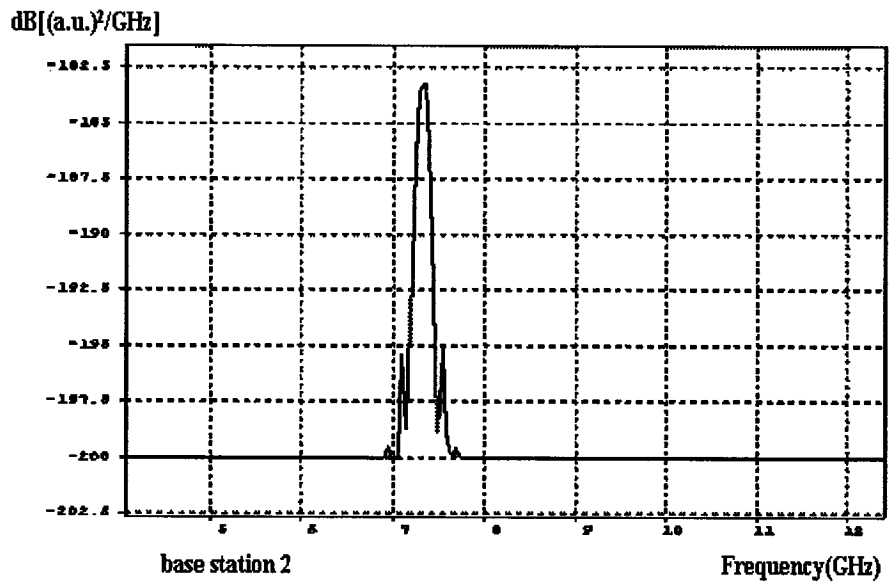


(f)

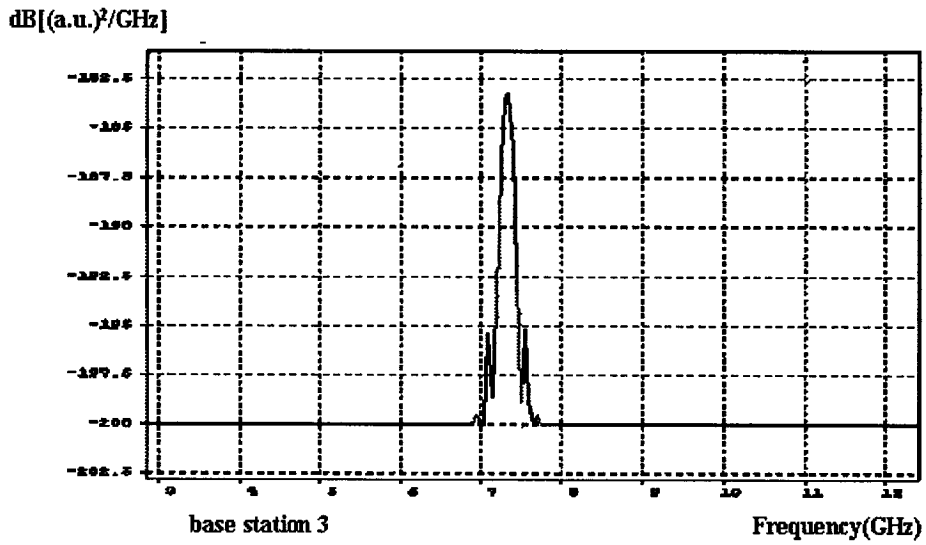


(g)

Figure 3.12 Electrical spectra after photodetection (e) base station 1, (f) base station 2, and (g) base station 3.

The Butterworth bandpass filter chosen with same reason as in the downlink selects the RF signal at frequency of around 7 GHz for DPSK demodulation. Table 3.9 lists the property of Butterworth bandpass filter.

Table 3.9 The property of Butterworth bandpass filter

| Base station | Central frequency (GHz) | 3dB bandwidth (GHz) |
|---|---|---|
| 1 | 7.36 | 1.2 |
| 2 | 7.34 | 1 |
| 3 | 7.3 | 1 |

The same demodulation scheme as the downlink demodulation is used in the uplink demodulation. So table 3.10 lists the property of the Bessel lowpass filter.

Table 3.10 The property of Bessel lowpass filter

| Base station | Number of poles | 3 dB bandwidth (GHz) |
|---|---|---|
| 1 | 5 | 0.1 |
| 2 | 5 | 0.1 |
| 3 | 5 | 0.1 |

### 3.2.4 Uplink Simulation Results

Figure 3.13 (a) shows the eye diagram observed while the received power at the photodiode is –41.65 dBm and the Q value is 40 dB. By comparing with the input data as shown in Figure 3.13 (b), the recovered data shown in Figure 3.13 (c) is very similar to the input data but the ripple of the "1" level and the distortion of the "0" level exist. Moreover, the curvature of the "1" level and the distortion of the "0" level are proportional to the ripple of the "1" level and the distortion of "0" level in the recovered data. Moreover, the noise accumulated by the optical combiner causes the distortion of the "0" level. By adjusting the bandwidth of the bandpass filter after the photodiode, the ripple can be reduced to the certain extent. In general, the error-free results are achieved in the uplink of the base station 1.

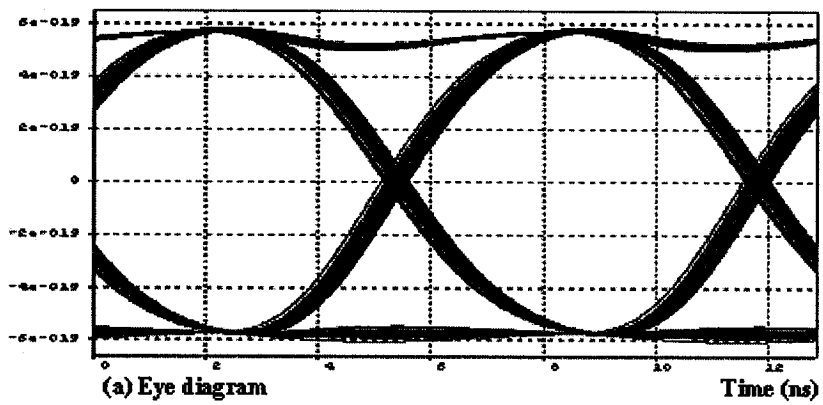

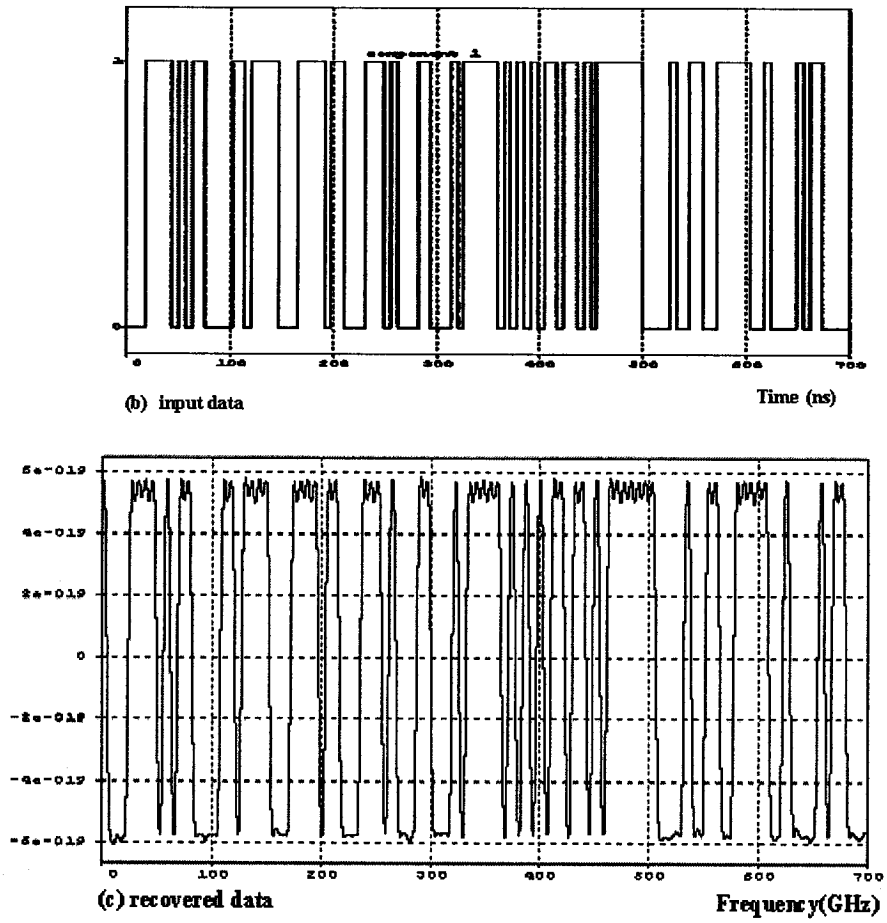


Figure 3.13 (a) eye diagram, (b) input data and (c) recovered output data in the base station 1

Figure 3.14 (a) shows the eye diagram observed while the received power at the photodiode is –50.29 dBm and the Q value is 40dB. Moreover, the ripple of "1" level as shown in Figure 3.14 (c) is reflected on the eye diagram by the curvature as well. By comparing with the input data as shown in Figure 3.14 (b), the recovered data shown in Figure 3.15 (c) is very similar to the input data but the phase is opposite. The possible reason is that the optical carrier $C_4$ replaces the optical carrier $C_2$ of the subcarrier $L_2^{uplink}$ and the DPSK coded data $\theta_{u2}(t)$ is delayed by $\beta_{d1,2}X_d + \beta_{u1,2}X_u$, which may cause

the recovered data to have the opposite phase. Moreover, the curvature of the "1" level on the eye diagram is proportional to the ripple of the "1" level in the recovered data. By adjusting the bandwidth of the bandpass filter, the ripple can be reduced to the certain extent. In general, the error-free results are achieved in the uplink of the base station 2.

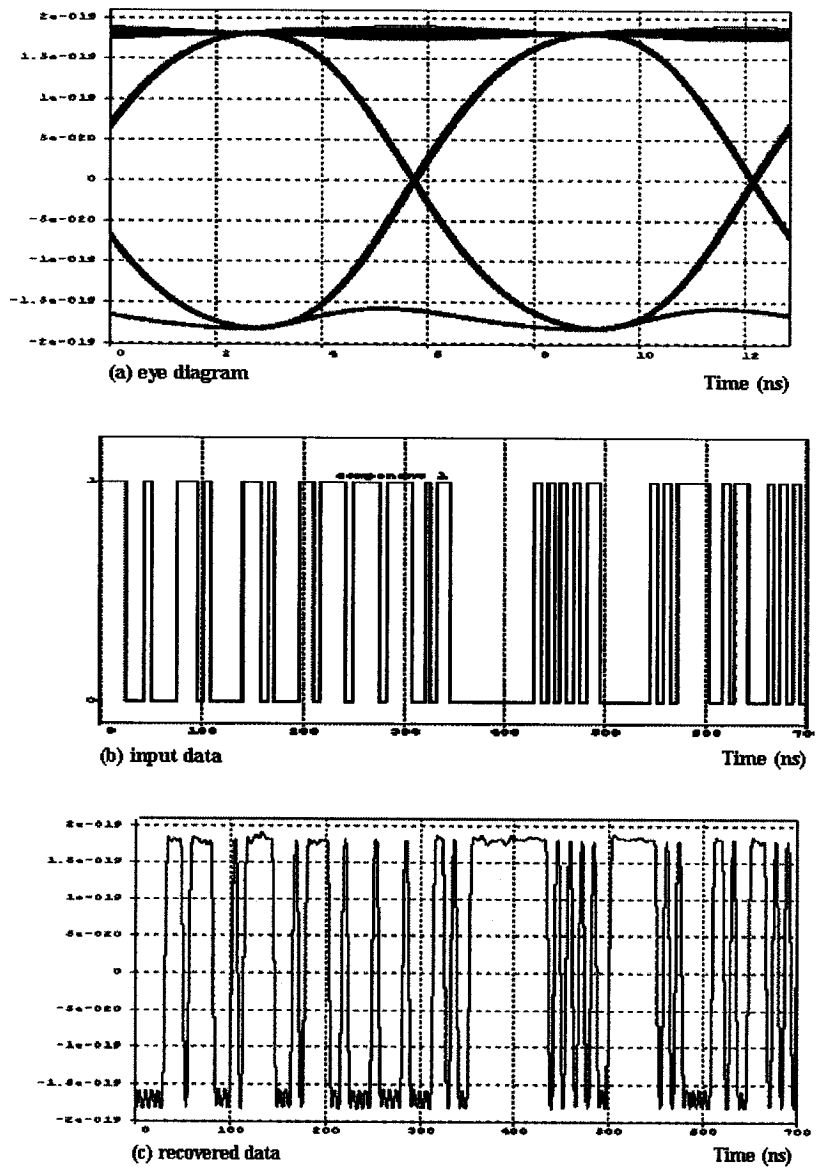


Figure 3.14 (a) eye diagram, (b) input data and (c) recovered output data in the base station 2

Figure 3.15 shows the results in the base station 3. The similar results as shown in Figure 3.14 are achieved except that the Q value is 40 dB while the received power is – 55.34 dBm. Like Figure 3.14, same phenomenon exists in figure 3.15.

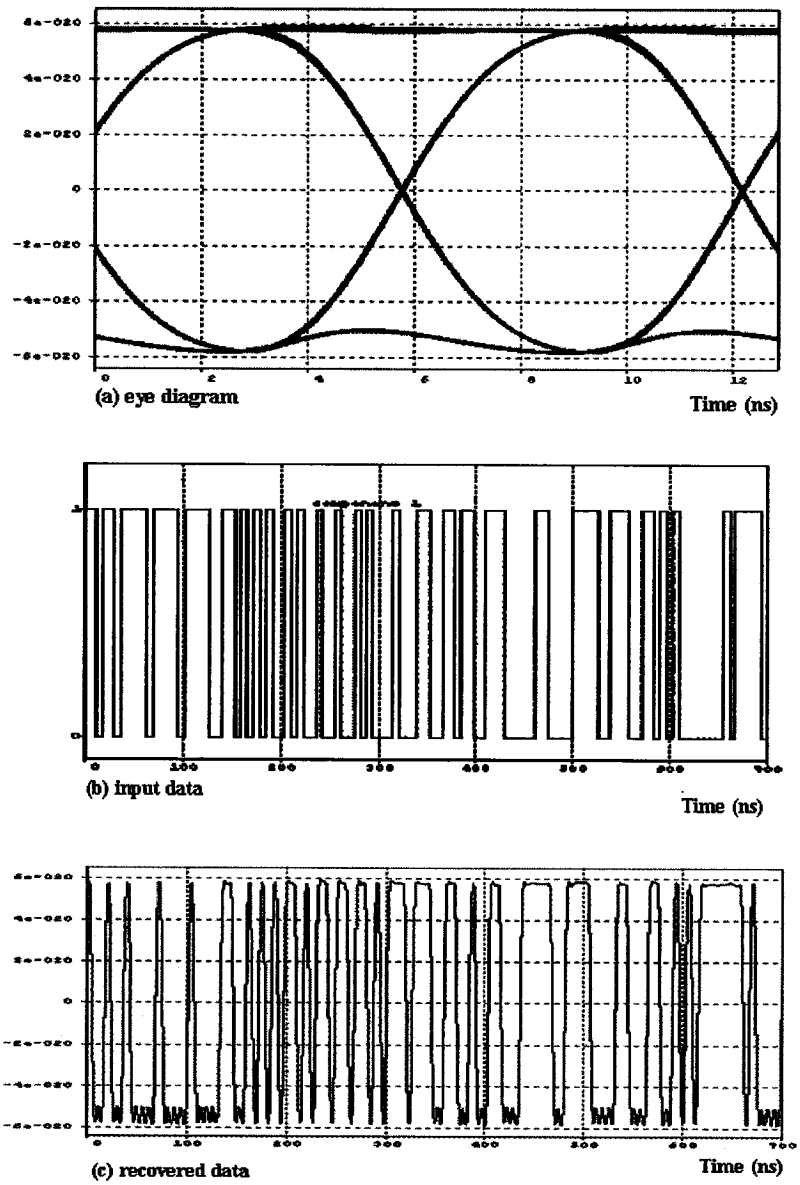


Figure 3.15 (a) eye diagram, (b) input data and (c) recovered output data in the base station 3

In general, the downlink system configuration and uplink system configuration are described. In the downlink direction, the configurations for MZ modulator, optical bandpass filter, electrical bandpass filter and lowpass filter are discussed. The downlink photodetection and DPSK demodulator are described as well. Moreover, the downlink simulation results are presented to show that the system operates successfully. On the other hand, in the uplink direction, the configurations for the optical narrowband bandpass filter and uplink modulation are described. The uplink photodetection by using the DWDM demultiplexing at the CS is discussed as well. Besides, the uplink simulation results are presented to demonstrate the uplink system operates successfully.

# Chapter 4 Discussion

## 4.1 Impact of Bandwidth of Electrical Bandpass Filter

The bandwidth of electrical bandpass filter is an important factor contributing to the performance of receiver. In order to investigate the impact of bandwidth, the simulation is performed with the different 3-dB bandwidth while keeping the type and central frequency of bandpass filter unchanged. By observing the distortion of the "1" level on the eye diagram and the ripple of the "1" level in the recovered data, the 3-dB bandwidth of the bandpass filter is optimized to reduce the ripple as small as possible.

Basically, in the demonstrated system, the 155.52 Mbps data with DPSK modulation occupies around 145 MHz at the 3-dB point as shown in Figure 4.1.

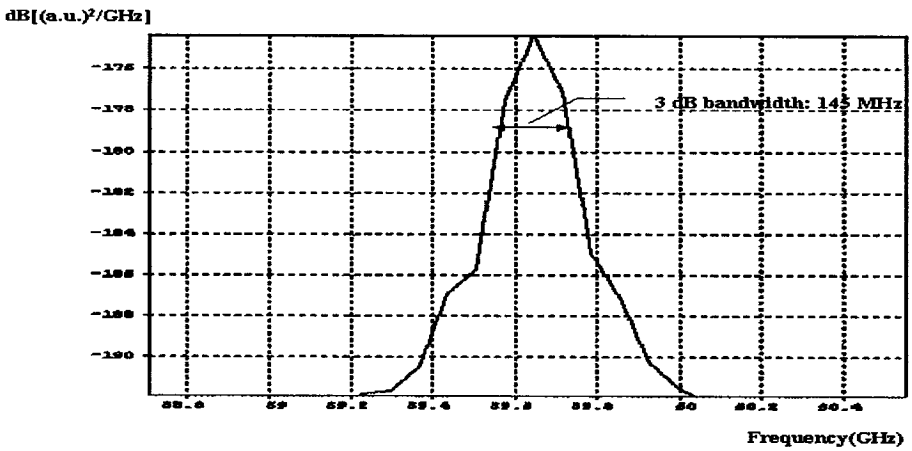


Figure 4.1 The spectrum to show the 3-dB bandwidth of 60 GHz signal with data rate of 155.52Mbps

However, if the 3-dB bandwidth, 300 MHz, is entered in the electrical bandpass filter to select the 60 GHz signal on the downlink and the 7 GHz signal on the uplink, the distortion of the "1" level on the eye diagram, which shown in Figure 4.2 (a), is observed. In addition, the ripple of the "1" level on the recovered data is appeared in Figure 4.2 (b), which is corresponding to the distortion of the eye diagram.

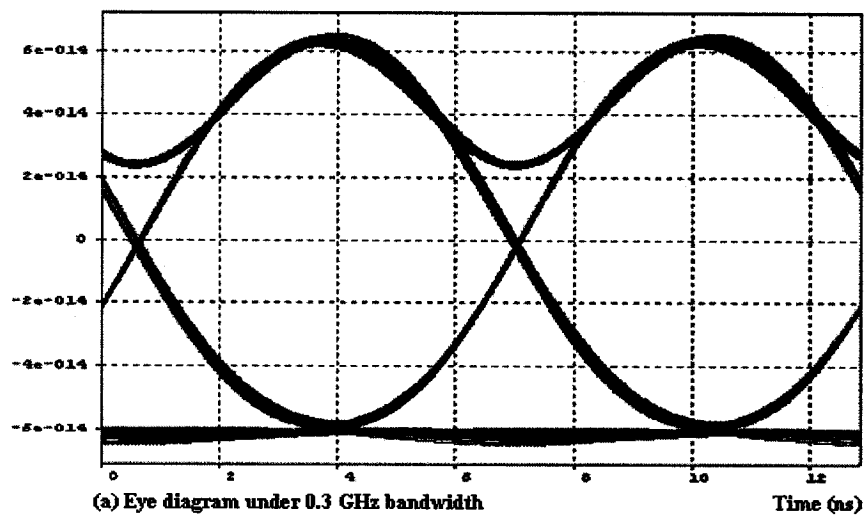

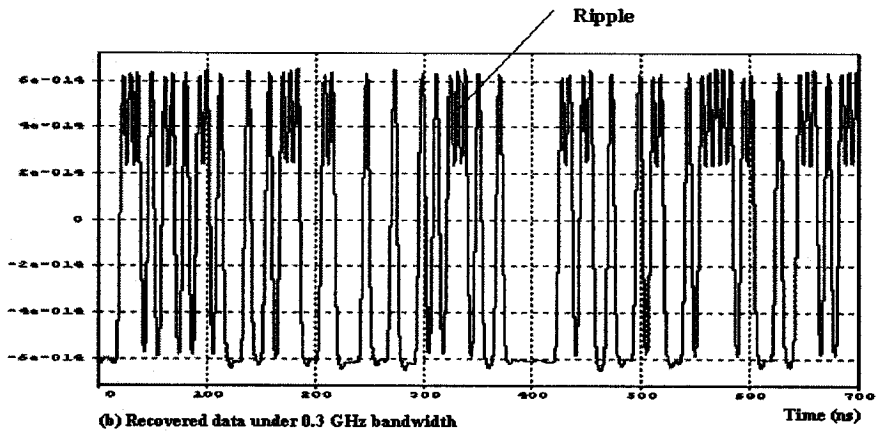


Figure 4.2 (a) Eye diagram under 0.3 GHz bandwidth; (b) Recovered data under 0.3 GHz.

In order to investigate the impact on the Q value, the simulation with the different bandwidth, 0.3 GHz, 0.5 GHz, 0.8 GHz, 1 GHz and 1.5 GHz, is performed. As shown in Figure 4.3, the variation of Q is not significant as the 3-dB bandwidth changes. There are about 4 dB changes from 0.3 GHz to 1.5 GHz.

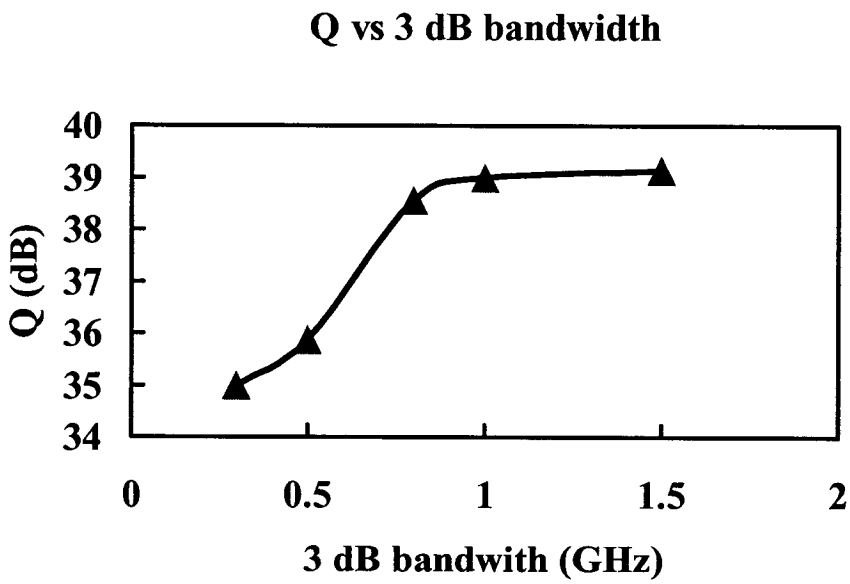


Figure 4.3 Q vs.3-dB bandwidth

However, the distortion of eye diagram has the significant improvement. The distortions as shown in Figure 4.4 (a) and (b) almost disappear and the ripples in Figure 4.4 (c) and (d) become smaller as the bandwidth is increased accordingly. Although the Q value is improved as well, the Q under the bandwidth of 0.3 GHz is still acceptable.

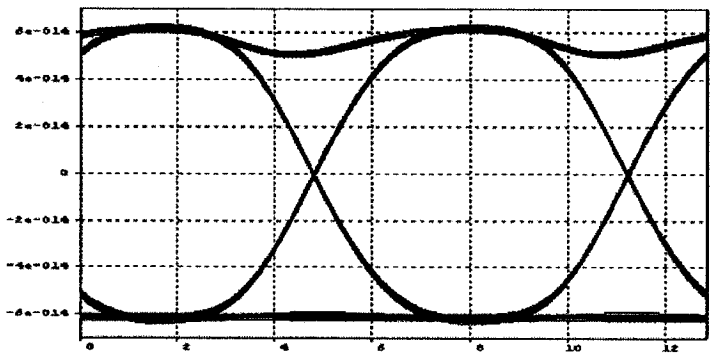

(a) Eye diagram under 1 GHz bandwidth

Time (ns)

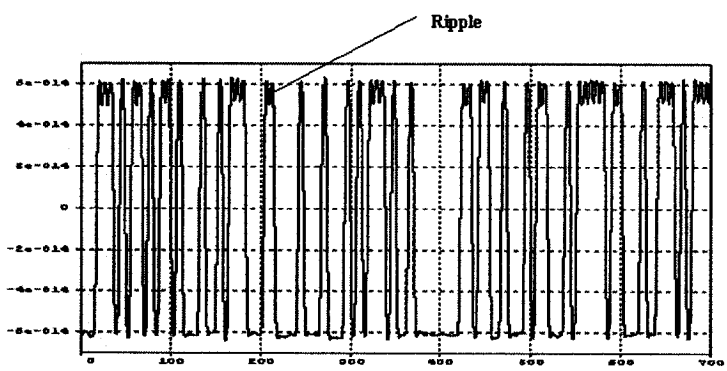


(b) Recovered data under 1 GHz bandwidth

Time (ns)

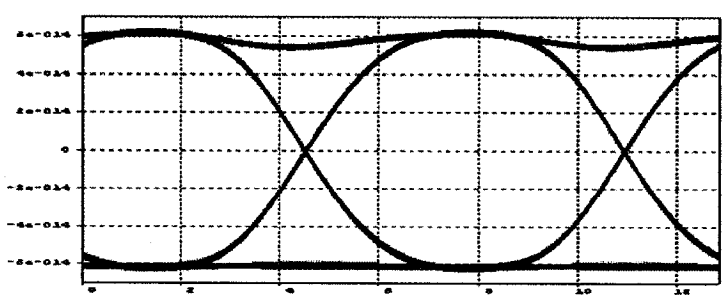

(c) Eye diagram under 1.5 GHz bandwidth

Time (ns)

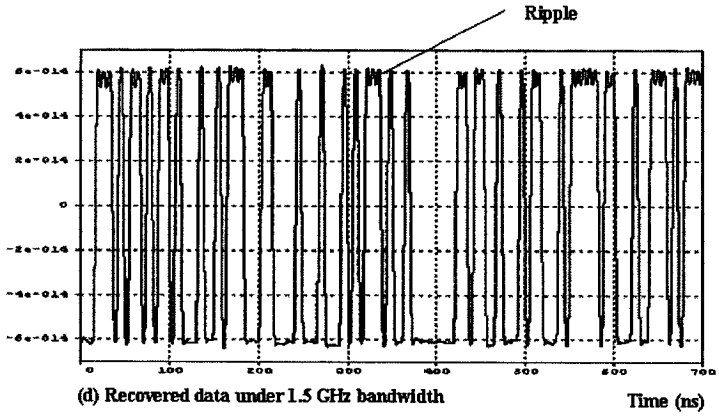


Figure 4.4 (a) Eye diagram under 1 GHz bandwidth; (b) Recovered data under 1 GHz bandwidth; (c) Eye diagram under 1.5 GHz bandwidth; (d) Recovered data under 1.5 GHz bandwidth.

In summary, the 3-dB bandwidth of bandpass filter affects the shape of the eye diagram and the Q value. In order to improve the appearance of the eye diagram, the bigger bandwidth than the measured 3-dB value has to be configured in the system. As an example, on the downlink, the bandwidth of bandpass filter in BS1, BS2 and BS3 is set up as 1.5 GHz, 2 GHz and 1.5 GHz, respectively. On other hand, on the uplink, the bandwidth of bandpass filter in BS1, BS2 and BS3 is set up as 1 GHz, 1 GHz and 1 GHz, respectively.

## 4.2 Impact of Laser Linewidth

The laser linewidth is a limiting factor in the demonstrated system. In order to compare with the demonstrated system, another system simulation is performed. The difference is that the RF signal, 10 GHz signal, is generated by the beating between the

optical carrier $C_3$ at $\lambda_3 = 1553.9nm$ and the LSB subcarrier $L_3$, which have the same laser phase noise term. The system configured with the linewidth of 100 MHz for the downlink transmission is shown in Figure 4.5.

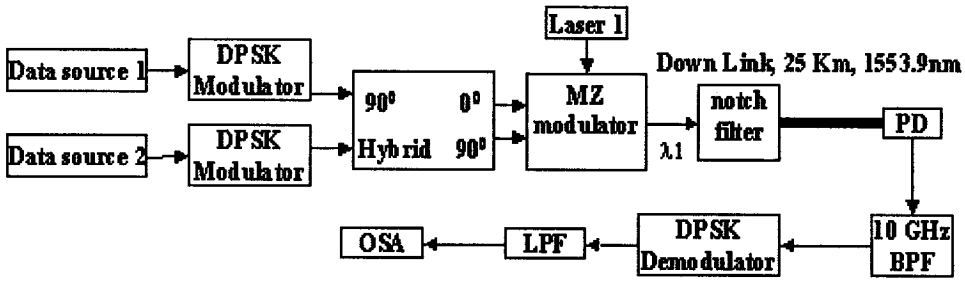


Figure 4.5 System configuration of single channel at $\lambda_3 = 1553.9nm$

Followed the derivation in section 2.1, after the square-law detection of a photodiode with the reference wavelength $\lambda_3 = 1553.9nm$ on the optical carrier $C_3$ in the BS, the photocurrent is given by

$$i_{c3,L3}(t, X_d) \propto 2\sqrt{2}Ra_{opt}P_{c3}J_0(\beta\pi)J_1(\beta\pi)\sin[\psi_{c3,L3}(t, X_d)] \quad (1)$$

Where, $R$ is the responsivity of a photodiode and then $\psi_{c3,L3}(t, X_d)$ is defined as

$$\psi_{c3,L3}(t, X_d) = \psi_{0,3}(t, X_d) - \psi_{-1,3}(t, X_d)$$

$$= 2\pi f_{d3}(t - \beta_{d1,3}X_d) + \theta_{d3}(t - \beta_{d1,3}X_d) - \frac{\pi}{4} \quad (2)$$

Hence, the laser phase term $\phi_{cn}(t)$ is cancelled in eq.(2). So the system can achieve the better performance with high tolerance of big linewidth. The simulation result shown in Figure 4.6 is obtained under the linewidth of 100MHz and the Q value is 18.18 dB.

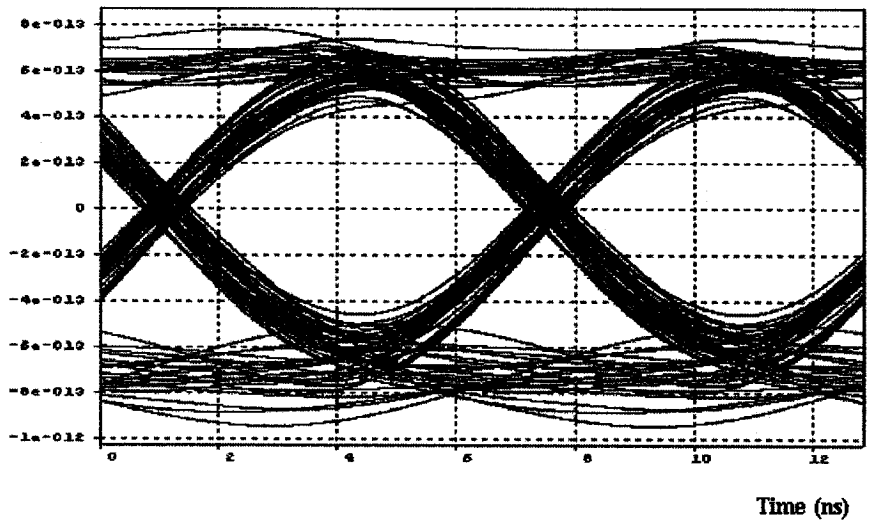


Figure 4.6 Eye diagram with the linewidth of 100MHz

However, the tolerance to the linewidth in the demonstrated system is weaker than the system described above. As an example, the eye diagrams in the base station 1 of the uplink as shown in Figure 4.7 indicates the degradation of the system performance. Figure 4.7 (a) shows the eye diagram with the Q value of 40 dB under the linewidth of 0 kHz and Figure 4.7 (b) shows the eye diagram with the Q value of 18.19 dB under the line width of 1 kHz. As noted, the linewidth is reduce from 100 MHz to 1 kHz with same Q value achieved.

In order to find out the tolerance to the linewidth for each base station, the simulation is performed and the result is shown in Figure 4.8. It is found out that the downlink has the strongest tolerance to the linewidth but the base station 1 of the uplink has the weakest tolerance to the linewidth. The base stations 2 and 3 have the tolerance in between. The possible reason why causes the inconsistency among the different uplink base stations is that the noise accumulated by the optical combiner which combines the

uplink signals together without any filter to suppress the noise level outside the uplink signal bandwidth of 57 GHz. In addition, there are no any uplink subcarriers modulated on the optical carriers $C_4$ and $C_5$ so the tolerance in the base stations 2 and 3 is better than the base station 1. As a result, the trade-off has to be done for each base station in order to optimize the value of linewidth depending on the Q or BER required.

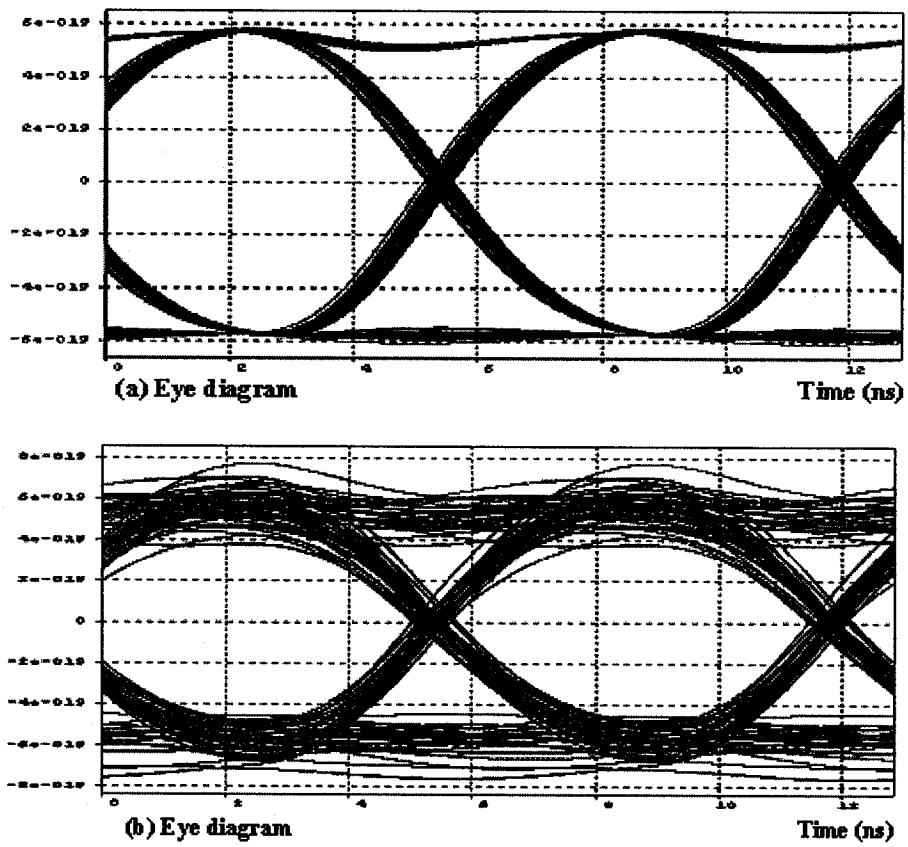


Figure 4.7 Eye diagrams (a) linewidth=0 kHz; (b) linewidth=1kHz.

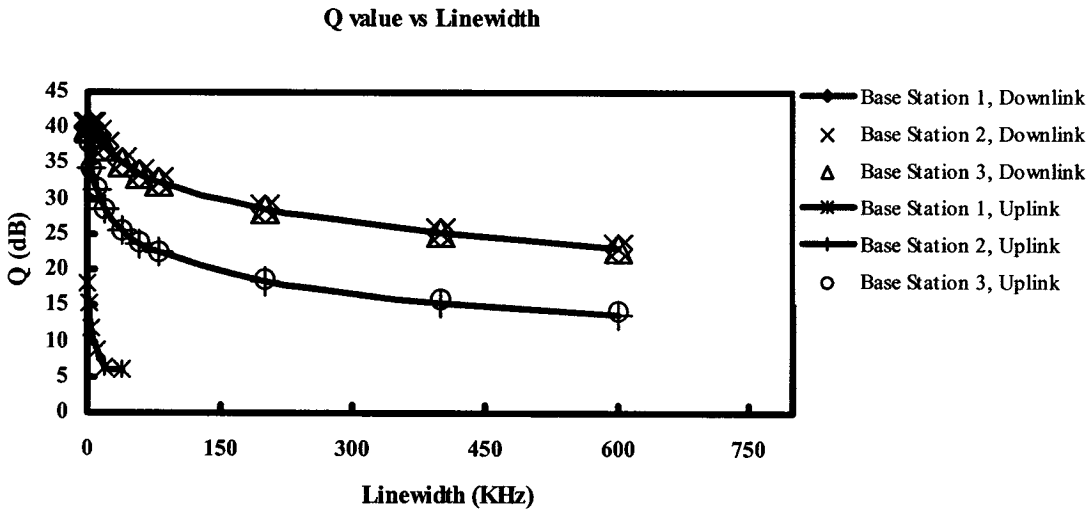


Figure 4.8 Q value vs. Linewidth

As an example, if the Q value of about 18 dB is acceptable for each base station in the demonstrated system, the linewidth of lasers at the wavelengths $\lambda_1 = 1553.5nm$, $\lambda_2 = 1553.7nm$, $\lambda_3 = 1553.9nm$, $\lambda_4 = 1554.1nm$ and $\lambda_5 = 1554.3nm$ are determined as 1 kHz, 200 kHz, 1 kHz, 200 kHz and 200 kHz, respectively. Even though the 800 kHz linewidth is allowed in BS2 or BS3 on the downlink, the lasers, which share with BS2 or BS3 on the uplink, bring this linewidth down to the 200 kHz in order to achieve the same Q value. Moreover, the linewidth of lasers, used for the BS1 on the downlink and the BS on the uplink, is reduced from about 800 kHz to 1 kHz because the channel in the BS1 of uplink is more sensitive to the linewidth (laser phase noise).

Comparing with the system described in Figure 4.5, the linewidth of lasers reduces from the 100 MHz to the 1 kHz or 200 kHz if the same Q or BER, 18 dB, is achieved. The reason is that the laser phase term $\phi_{cn}(t) - \phi_{c(n+2)}(t)$ in eq.(24) cannot be neglected because it originates from two different light sources and results from the

replacement of the optical carrier of the LSB subcarrier. This causes the degradation of the receiver performance and further put the limitation on the laser specification. Therefore, it concludes that the high quality lasers with smaller linewidth are required in the demonstrated system. However, note that the conclusion is obtained from the DPSK signal in the demonstrated system. If the system uses the amplitude shift keying (ASK) signal or the frequency shift-keying (FSK) signal, the laser phase noise may not be a limiting factor.

In conclusion, the impact of bandwidth of electrical bandpass filter and the impact of linewidth are investigated. The bandwidth of electrical bandpass filter is a contributing factor to the shape of eye diagram and has an impact on the Q value as well. It is found out that the bandwidth bigger than the 3-dB value has to be used in the bandpass filter. As another limiting factor, the linewidth degrades the system performance because the RF DPSK modulation is tested in the demonstration system. However, the optimization of linewidth can be determined by the Q value to be achieved.

# Chapter 5 Conclusion

The full-duplex star-tree DWDM system is simulated and the concept of the new approach incorporating the channel spacing of 25 GHz in DWDM is successfully proven, which improves the optical spectral efficiency. Also, the generation of the 60 GHz signal is accomplished without the involvement of either the photonic downconversion (PDC) or the dual mode light. More importantly, the 60 GHz signal is converted from the lower radio frequency signals, for instance 10 GHz in the demonstrated system. So the cost-effective DPSK modulator with the lower radio frequency can be used in the CS. By observing the eye diagram, the error-free results are simultaneously achieved on the downlink and uplink transmission. Further, the impact of the electrical bandpass filter to the receiver performance is investigated by comparing the eye diagram and recovered

data with different bandwidth scenarios. The result concludes that the bandwidth is wider than the 3-dB bandwidth in order to achieve the better eye diagram. Besides, due to the different light sources of beating signals that generate the 60 GHz signal in the downlink and the 7 GHz signal in the uplink, the system performance is limited by the laser phase noise. However, the high quality laser could be a solution to resolve this issue. Although the high quality lasers are required in the CS, the demonstrated system is still cost effective because the remote light sources are used in the BSs. However, note that the laser phase noise limits the performance of system using DPSK modulation but it may not affect the performance of the system using ASK or FSK modulation. Provided that the asymmetric Fabry-Perot modulator [18] as a variation of EA modulators could be fabricated in the future, the BS in the demonstrated system is not far from reality of becoming the maintenance-free and passive.

## References


[1] P. Smulders, "Exploiting the 60 GHz band for local wireless multimedia access: prospects and future directions," *IEEE Communications magazine*, pp.140-147, January 2002

[2] T. Kuri, and K. Kitayama, "Optical heterodyne detection technique for densly multiplexed millimeter-wave-band radio-on-fiber systems," *J. lightwave technol.*, vol.21, pp.3167-3179, December 2003

[3] C. Lim, A. Nirmalathas, D. Novak, and R. Waterhouse, "Capacity analysis for WDM fiber-radio backbones with star-tree and ring architecture incorporating wavelength interleaving," *J. lightwave technol.*, vol.21, pp.3308-3315, December 2003

[4] T. Kuri, K. Kitayama, and Y. Takahashi, "Simplified BS without light source and RF local oscillator in full-duplex millimeter-wave radio-on-fiber system based on external modulation technique," *IEEE Int. Microwave Photonics Topical Meeting Technical Dig.*, pp. 123-126, 1999

[5] T. Kuri, K. Kitayama, and Y. Takahashi, "A single light-source configuration for full-duplex 60-GHz-band radio-on-fiber system," *IEEE Trans. Microwave Theory Tech.*, vol.51, pp.431-439, February 2003

[6] A. Nirmalathas, C. Lim, D. Novak and R.Waterhouse, "Optical interfaces without light source for base-station designs in fiber-wireless systems incorporated WDM," *IEEE Int. Microwave Photonics Topical Meeting Technical Dig.*, pp.119-122, 1999

[7] D.Wake, D.Johansson, and D.G. Moodie, "Passive picocell: a new concept in wireless network infrastructure," *Electronic Letters*, vol. 33, pp. 404-406, February 1997

[8] G.H. Smith, D.Novak, and Z.Ahmed, "Overcoming chromatic dispersion effects in fiber-wireless system incorporating external modulators," *IEEE Trans. Microwave Theory Tech.*, vol. 45, pp. 1410-1415, August 1997

[9] T. Kuri, H.Toda, and K. kitayama, "Dense wavelength-division multiplexing millimeter-wave-band radio-on-fiber signal transmission with photonic downconversion," *J.lightwave technol.*, vol 21, pp. 1510-1517, June 2003

[10] K. Kitayama, T. Kuri, K. Onohara, T. Kamisaka and K. Murashima, "Dispersion effects of FBG filter and optical SSB filtering in DWDM millimeter-wave fiber-radio systems," *J. lightwave technol.*, vol.20, pp.1397-1407, August 2002

[11] T. Kuri, K. Kitayama, A. Stohr, and Y. Ogama, "Fiber-optic millimetre-wave downlink system using 60-GHz-band external modulation," *J. lightwave technol.*, vol.17, pp.799-806, May 1999

[12] R.Hui, "Multi-tribuary OFDM optical transmitter using carrier-suppressed optical single-sideband modulation," *OFC'2003*, vol.1, pp 92-93, March 2003

[13] R. Hui, B. Zhu, R. Huang, C. T. Allen, K. R. Demarest and D. Richards, " Subcarrier multiplexing for high speed optical transmission," *J. lightwave technol.*, vol.20, pp.417-427, March 2002

[14] G.P. Agrawal, *Nonlinear Optics*, 2nd ed. New York: Academic, 1995, sec.2 to 4.

[15] T. Kuri, K. Kitayama, and Y. Ogawa, "Fiber-optic millimeter-wave uplink system incorporating remotely fed 60-GHz-band optical pilot tone," *IEEE Trans. Microwave Theory Tech.*, vol. 47, pp. 1332-1337, July 1999

[16] K. Kitayama, "Architectural consideration of radio-on-fiber millimeter-wave wireless access system," *Fiber Integr.Opt*, vol. 19, pp.167-186 2000

[17] G.P. Agrawal, *Fiber-optic communication system*, 3rd ed. New York: A John Willey & Sons., 2002, chapter 10.

[18] C. P. Liu, A. J. Seeds, J. S. Chadha, P. N. Stavrinou, G. Parry, M. Whitehead, A. Krysa and J. S. Roberts, "Normal-incidence 1.56-um MQW asymmetric Fabry-Perot modulator (AFPM) for passive picocell," *International Topic Meeting on Microwave Photonics*, pp.49-52, November 2002